Low-Energy Proton Accelerator for Detector Testing

by

David Harrison

A Thesis submitted to the Faculty of Graduate Studies of

The University of Manitoba

in partial fulfilment of the requirements of the degree of

MASTER OF SCIENCE

Department of Physics and Astronomy

University of Manitoba

Winnipeg

I would like to dedicate this thesis to my wonderful family for their support throughout my years as a physics student.

Abstract

Future fundamental physics experiments in neutron beta-decay require highly efficient detection of protons. Many of the experiments use electrostatic acceleration of the recoil protons into large-area silicon detectors for this purpose. A 30 keV proton accelerator was designed, created, and commissioned in order to characterize silicon detectors of this type. Final construction and initial results on the performance of the accelerator are presented. A unique aspect of the work is the use of a Penning ion generator as an ion source. The accelerator produced protons with momentum resolution $\sim 1\%$. The ion source produced current stably, over a range of parameters, and over long periods of time. The accelerator achieved proton rates sufficient to calibrate silicon detectors.

Acknowledgements

Thank you to all those who helped with this thesis project. In particular significant assistance was provided by undergraduate students Graham Schellenberg and Nick Macsai who both helped with the operation of the proton accelerator as well as various projects associated with this thesis.

Table of Contents

List of Figures

List of Tables

Chapter 1

Introduction

1.1 Overview

Particle detection is an essential component of experimental subatomic physics. Experiments place requirements on detector efficiency, energy resolution, and response time. The technology used to effectively detect particles depends on particle type and energy.

The construction of a proton calibration source for detectors of protons resulting from neutron decay is the main interest of this thesis. Free neutrons decay into a proton, an electron, and an electron antineutrino. The detection of antineutrinos is impossible in present experiments, so precision experiments in neutron decay detect either the decay electron, proton, or both. From the kinematics of the decay, the recoil proton from neutron decay possesses little kinetic energy relative to the decay electron. Recoil protons are therefore typically accelerated to tens of keV energies in order to facilitate detection. The focus of this thesis is the creation of a testbed to characterize the detectors used to observe protons in the ~ 30 keV energy range.

1.2 Neutron Decay

Neutron decay is of modern interest for both astrophysical and fundamental physics reasons [1, 2].

In astrophysics, neutron decay is important in Big Bang Nucleosynthesis [3] and in solar fusion [4]. In BBN, primordial neutrons and protons form into heavier elements such as deuterium and helium. Precise measurements of the neutron lifetime are therefore important for accurate predictions of the relative abundances of the light elements [5].

The study of neutron decay also allows for precision tests of the electroweak sector of the standard model of particle physics [1, 2]. Neutron decay is mediated by the weak nuclear force and is described by the Feynman diagram shown in Fig. 1.1. The diagram shows an initial state neutron as one up and two down quarks. In electroweak theory, one of the down quarks is converted into an up quark by emitting a virtual W^- boson. The result is a proton with two up and one down quark and the virtual W^- boson which subsequently decays into an electron and an anti-neutrino. In the Feynman rules for electroweak theory, the quark-W^- vertex receives a factor V_{ud}, which is an element of the Cabibbo-Kobayashi-Maskawa (CKM) matrix. It is a long-term goal of studies of neutron decay to determine V_{ud} precisely from neutron decay.

Presently, this parameter of the standard model is most precisely determined from $0^+ \rightarrow 0^+$ superallowed nuclear decays [6, 7]. Measurements employing neutron decay are presently statistically limited compared to the nuclear measurements. However, as neutron sources are developed with increasing fluxes, the potential for improved statistical precision has continued to increase. The neutron measurements would offer a new window on V_{ud}, with the extraction being free of nuclear corrections.

Knowledge of the parameter V_{ud} is important for a variety of unitarity tests in the stan-

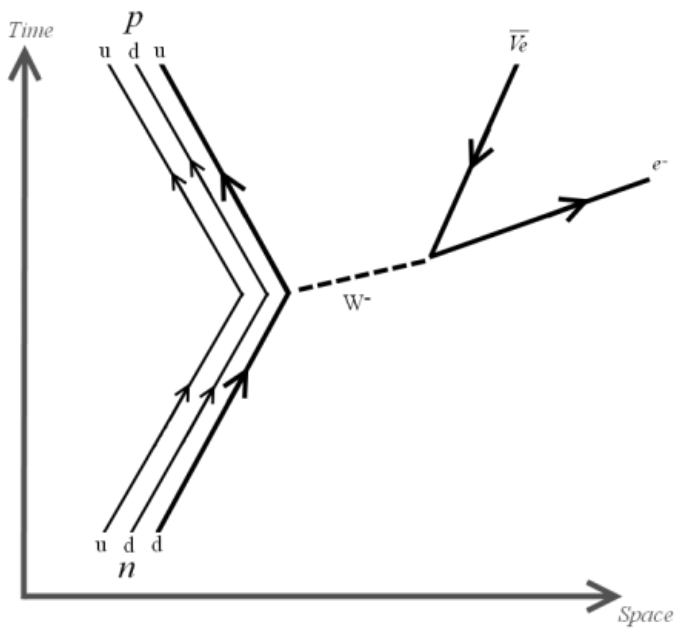

Figure 1.1: Feynman diagram for neutron decay in electroweak theory.

dard model, the most precise one being a test of $|V_{ud}|^2 + |V_{us}|^2 + |V_{ub}|^2 = 1$. Here, V_{us} and V_{ub} would be determined from weak decays of systems containing s and b quarks to u quarks. Presently, the value of this unitarity test is $|V_{ud}|^2 + |V_{us}|^2 + |V_{ub}|^2 = 0.9999 \pm 0.0006$ [7]. The uncertainty is dominated relatively equally by the experimental precisions on V_{ud} and V_{us}. Neutron experiments reaching sufficient precision could therefore have an important impact on the field. New physics would enter this process through loop effects that could modify the quark-W^- vertex (see e.g. calculations performed in the context of supersymmetry in Refs. [8–10]), which could in turn result in a violation of the unitarity test.

We now briefly discuss the sensitivity of neutron decay to V_{ud}.

1.2.1 Axial and vector couplings, and V_{ud}

Experimental studies of angular correlations in neutron decay allow for sensitive measurements of the ratio of axial vector to vector coupling constants $\lambda = G_A/G_V$. The present value recommended by the Particle Data Group is $\lambda = -1.2701 \pm 0.0025$ [7].

The value of G_A is modified by the strong interaction, and it is therefore of interest in testing quantum chromodynamics (QCD). The value of G_V is protected by the conserved vector current (CVC) hypothesis. Its value is therefore related to the fundamental quark-W^- coupling and hence V_{ud} [1, 6]. Measurements of λ can be combined with measurements of the neutron lifetime τ_n in order to separately extract G_A and G_V and hence evaluate V_{ud} using only neutrons [1].

Neutron decay was described in the seminal paper by Jackson, Treiman and Wyld [11]. The triple differential neutron decay rate is entirely determined by five dimensionless parameters a, b, A, B, and D, as:

$$\frac{dw}{dE_e d\Omega_e d\Omega_\nu} \propto p_e E_e (E_0 - E_e)^2 \times \left[1 + a\frac{\vec{p_e}\cdot\vec{p_\nu}}{E_e E_\nu} + b\frac{m_e}{E_e} + \langle\vec{\sigma_n}\rangle \cdot \left(A\frac{\vec{p_e}}{E_e} + B\frac{\vec{p_\nu}}{E_\nu} + D\frac{\vec{p_e}\times\vec{p_\nu}}{E_e E_\nu}\right)\right] \quad (1.1)$$

where nucleon recoil and radiative corrections have been neglected. Here, $\vec{p}_{e,\nu}$ and $E_{e,\nu}$ are the electron and electron antineutrino momenta and energies respectively, $\vec{\sigma}_n$ is the neutron spin, and E_0 is the beta spectrum endpoint. The total decay rate w is related to the neutron lifetime τ_n via $w = 1/\tau_n$.

Measurements using polarized neutrons yield the coefficients A, B and D while the coefficients a and b may be determined using unpolarized neutrons. Simultaneous measurements of proton and electron kinematics are required to constrain neutrino kinematical quantities in Equation (1.1). Assuming that G_A and G_V are real constants then A, B and a

can be expressed to first order in terms of λ (as in Ref. [1]):

$$A = \frac{-2\lambda\,(\lambda + 1)}{1 + 3\lambda^2} \tag{1.2}$$

$$B = \frac{2\lambda\,(\lambda - 1)}{1 + 3\lambda^2} \tag{1.3}$$

$$a = \frac{1 - \lambda^2}{1 + 3\lambda^2} \tag{1.4}$$

The triple decay coefficient D is zero under the assumption of time reversal invariance, and the coefficient b is zero in the standard model (i.e. in the nonexistence of scalar and tensor currents, as described in Ref. [11]).

The current world average values for the A, B, and a coefficients are summarized in Table 1.1.

Parameter	Value
A	-0.1176 ± 0.0011
B	0.9807 ± 0.0030
a	-0.103 ± 0.004

Table 1.1: Particle data group values of selected decay correlation coefficients from Ref. [7].

Given equations (1.2)-(1.4), and the present best experimental values in Table 1.1, the quantity λ is best constrained by measurements of the beta-asymmetry, i.e. the experimentally determined parameter A. This experiment does not require proton detection since it is formed from a correlation between the electron momentum and neutron spin. However, future experiments aim to determine a, and at times all three parameters A, B, and a to higher precision, in order to provide the best possible extraction of λ. In Section 1.3, we focus on some details of the Nab experiment, which aims to constrain a to high precision. Since this is a beta-neutrino correlation, proton detection is necessary.

Experiment	Decay Parameters Measured	Status
abBA	a, b, B, A	Future
aCORN	a	Future
aSPECT	a	Future
emiT-III	D	Completed, Future
Nab	a, b	Future
NIST Penning Trap	τ_n	Upgrading
PENeLOPE	τ_n	Future
PERKEO-III	A, later A, B	Commissioning
UCNB	A, B	Commissioning

Table 1.2: Selected present and future experiments on neutron β decay requiring proton detection.

1.3 Neutron decay experiments involving proton detection

Many ongoing and future neutron decay experiments are reliant on proton detection to achieve their physics goals. A few examples are: abBA [12], aSPECT [13], PERKEO-III [14], UCNB [15], emiT [16], PERC [17], aCORN [18], PENeLOPE [19], the Penning trap lifetime experiment at NIST [20], and Nab [21–23]. The goals of the experiments in terms of the decay parameters they aim to constrain, and their present experimental statuses, are presented in Table 1.2. It is clear from the Table that there are a large number of presently running or proposed experiments interested in the detection of protons resulting from neutron decay. The results of this thesis would therefore be of general interest to a large number of neutron physicists.

Our research group is involved in the Nab experiment, and so a few further details of that challenging experiment are discussed here. The Nab experiment could be considered a prototypical experiment embodying many common features of the other apparatuses.

The Nab experiment is a future experiment to be conducted on the Fundamental Nuclear Physics Beamline (FNPB) at the Spallation Neutron Source (SNS, Oak Ridge, TN, USA).

The aim of the experiment is to measure the coefficients a and b in unpolarized neutron decay to higher precision than ever before.

Measurement of a requires measurement of the electron energy and the proton momentum for each neutron decay. Measurement of b requires a measurement of the electron energy spectrum; b would manifest as a modification of this spectrum.

A schematic for the original idea for the Nab spectrometer is shown in Fig. 1.2. The

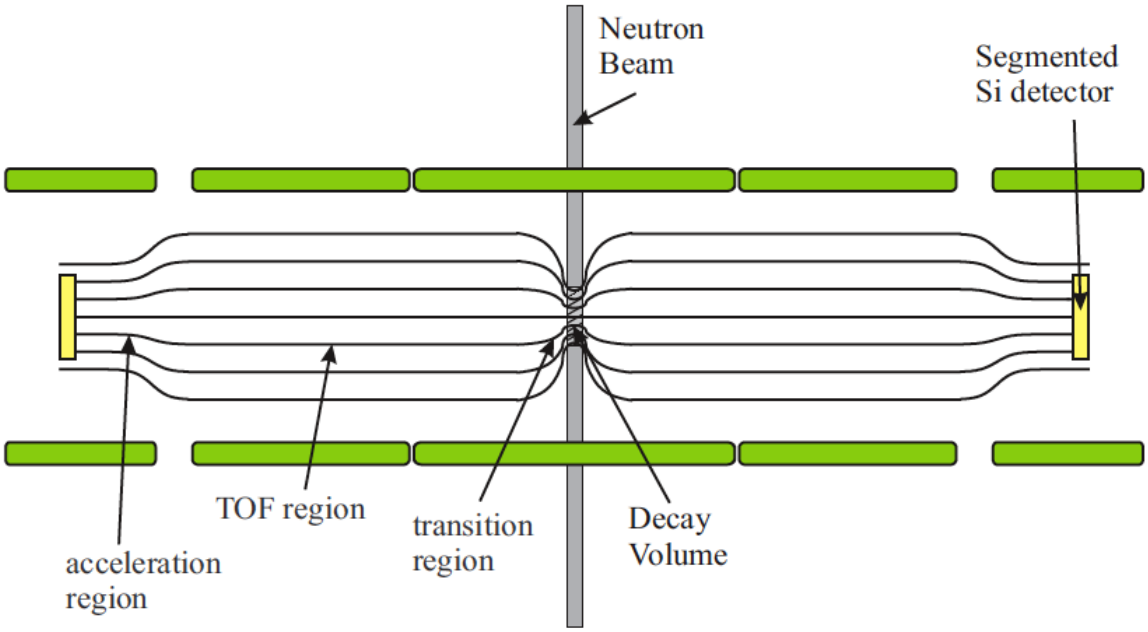

Figure 1.2: Schematic diagram of the Nab field expansion spectrometer in its original design (used for purposes of illustration, and design principles discussed in the text). The spectrometer consists of a decay volume followed by a field expansion to a time-of-flight (TOF) region, followed by an acceleration region just before the detectors [22]. The lines in the in the diagram represent the magnetic field.

measurement will be performed using silicon detectors in a field expansion spectrometer to detect both protons and electrons resulting from decay in flight from a pulsed beam of cold neutrons.

Neutrons decay in the central decay volume. Decay protons and electrons are harvested

by the magnetic field, spiraling around the field lines until they are sensed by detectors at either end of the spectrometer.

The magnetic field expansion decreases the angle between the particles and the magnetic field lines so particles strike the detectors at near normal incidence. This alignment is due to the requirement to maintain an adiabatic invariant, $p_p erp^2/B$, where $p_p erp$ is the momentum perpendicular to the spiral motion. Just before the detectors an accelerating potential of 30 keV is applied giving the protons sufficient energy to be detected. This 30 keV accelerating potential sets the energy scale for the proton accelerator which is being discussed in this thesis. The detectors are large area segmented silicon detectors and are discussed in more detail in Chapter 2.

The key feature of Nab is the use of a time-of-flight (TOF) technique to measure a. Electron-proton coincidences are sensed by the detectors. The electron strikes the detectors essentially instantaneously, moving at a considerable fraction of the speed of light. The proton is nonrelativistic and consequently moves more slowly through the field expansion region. In this region, the proton momentum becomes almost parallel to the magnetic field lines. The time it takes for the proton to traverse this region therefore becomes a good measure of the magnitude of the proton momentum, as opposed to the direction of proton emission. Because the field expansion region is long compared to the other regions, and because the electron is relativistic, the electron-proton time difference is dominated by the time the proton spends in this region.

The combination of measuring the electron energy E_e and magnitude of proton momentum p_p is sufficient to constrain the kinematics in order to determine a. It happens that a may be essentially determined by binning the decay rate in p_p^2 for a given E_e and measuring the slope of the distribution in p_p^2.

A new asymmetric spectrometer design is now being pursued by the collaboration,

where one detector package is very close to the neutron beam, and the other is far away at the end of a single field expansion region [23]. The design calls for a longer flight path of the protons, offering increased sensitivity to the proton momentum. The protons must now also pass through a field pinch prior to entering the field expansion region. This accepts protons whose decay angles are such that the proton momentum is already nearly parallel to the to the magnetic field lines, and therefore within the field expansion region, the proton momentum is even closer to parallel to the magnetic field lines. These changes, in all, give increased statistical sensitivity of the apparatus to a with decreased systematic error. Ultimately a determination of the a parameter at the 0.1% level is possible with the new spectrometer design.

Coincident proton detection is also believed to be essential for reducing backgrounds, for the accurate determination of b [23]. The parameter b is determined from precise electron spectroscopy.

Accurate proton detection with good timing is therefore crucial for the success of the Nab experiment.

1.4 Other proton sources for calibration of proton detectors for neutron decay experiments

Other neutron decay experimenters have constructed proton accelerators for the purpose of calibrating proton detectors. We briefly review two of these efforts. These are the Proton Accelerator for Femtoampere Flux (PAFF) [24], and a proton source constructed at North Carolina State University (NCSU) by Seth Hoedl [25].

The PAFF accelerator provided proton beam in the 10 keV to 35 keV region with

currents ranging from tens of protons per second to ~nA proton current. PAFF used a filament-based ion source located in a high voltage cage, followed by a 30° ion separation spectrometer magnet, an Einzel lens, a multichannel plate monitor region, and finally a detector region which could be used for detector tests.

The accelerator at NCSU had an energy range of 25 keV to 40 keV and provided currents in the region of 100 to 100k protons/s. It used a similar source, accelerator, spectrometer, and focusing arrangement as PAFF.

There are two principal differences between our approach and the approaches of Refs. [24, 25]. The first difference is our use of a Penning ion generator (PIG) source of protons, as opposed to a filament-based source. In this regard, our proton source is based on the design of Ref. [26].

This kind of source does not involve any filament. A stable arc current is struck which creates a plasma in a magnetic field provided by permanent magnets internal to the source. The potential advantages of this simple design are that it provides a robust, low maintenance source, with a stable current of protons.

In Ref. [26], their PIG was constructed from an iron cathode body, a samarium cobalt permanent magnet, a stainless steel anode, and an iron cathode faceplate. Their PIG source was capable of generating a plasma discharge yielding a 1 mA beam of H^+ ions with a source pressure of ~1 mTorr, using arc voltages in the range $1 - 6$ kV.

The second difference in our approach is the use of a pre-existing high-resolution mass spectrometer to analyze the ions produced by the source and select protons. Our apparatus is described in detail in Chapter 3.

Chapter 2

Theory

2.1 Overview

The goal of this Chapter is to review, from a more theoretical standpoint, the operation of two key components of the apparatus:

- the mass spectrometer, and
- the silicon detectors.

2.2 Ion Optics

The operation of mass spectrometers may be described to first order following the theory of Herzog [27]. An effective summary of the theory and its use in the design of mass spectrometers is provided in Ref. [28]. A summary of the relevant elements of the first-order ion focusing theory are reviewed in this Section. Further higher order calculations may be found in Ref. [28].

Our spectrometer consisted of both a magnetic spectrometer and an electrostatic analyzer. We therefore begin by reviewing ion optics in the relevant field configurations. We then review how the combination of these elements can give rise to an interesting double-focusing solution where focusing occurs in both velocity and position. The original design of the Manitoba-II mass spectrometer is based on the application of these same ideas, but in higher order.

2.2.1 First order optics in a homogeneous sector magnet

We begin with the case of a homogeneous magnetic field. Fig. 2.1 provides a diagram which defines relevant variables. Ions with mass M_0 and velocity v_0 are emitted from

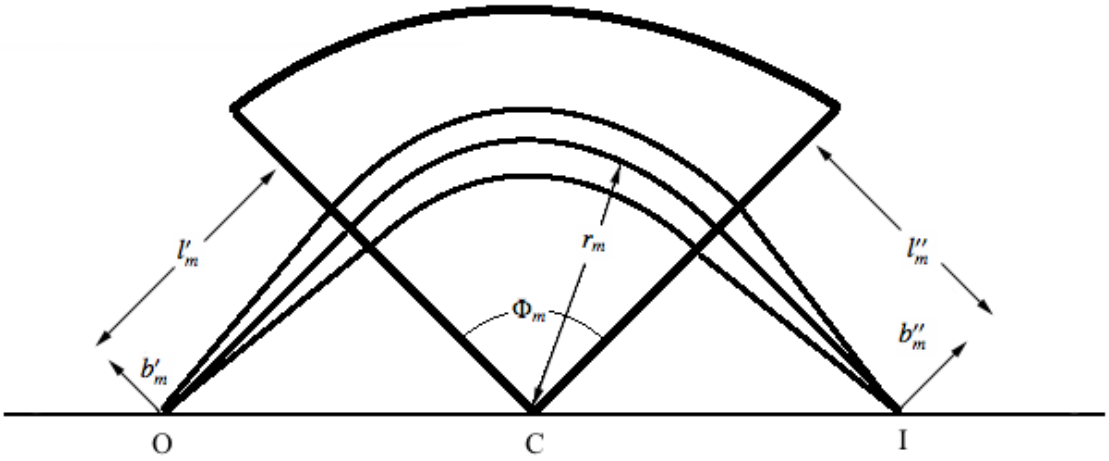

Figure 2.1: First-order ion optics in a homogeneous magnetic field for a magnetic sector of angle Φ_m (after Ref. [28]). Ions emitted from object point O are focused to the image point I. The magnetic field points out of the page within the pie-shaped region, and is zero elsewhere. Other variables are described in the text.

object point O at various angles α relative to the central (median) path.

An ion following the median path travels a distance l'_m before entering the magnetic field with normal incidence. The ion then follows a circular path of radius r_m with the

center of the radius of curvature at point C. During the course of its passage through the magnetic field, the ion deflects through angle Φ_m, emerging normally from the magnetic field region. It then travels a distance l''_m, arriving at the image point I.

The basic reason for sector focusing can be understood by considering the two paths shown on either side (upper and lower) of the median path in Fig. 2.1. The common feature of all three paths is that the radius of curvature in the magnetic field r_m is the same. What is not common is the origin from which the radius of curvature acts. For the upper path, the centre of the radius of curvature is displaced upward from point C. The ion therefore traverses a longer distance in the magnetic sector, and is diverted through a larger angle than the median path, so that it eventually arrives at point I. For the lower path, the center of the radius of curvature is displaced downward from point C and the ion is diverted through a smaller angle, having traversed a smaller distance in the magnetic sector.

Ions not traveling along the median path are focused to the image point as long as certain conditions are met. Ref. [27] gives the focal length f_m for this arrangement of magnetic field to be:

$$f_m = \frac{r_m}{\sin \Phi_m}. \tag{2.1}$$

In optics, the object and image distances are related by the focal length by a product according to

$$(l'_m - g_m)\,(l''_m - g_m) = f_m^2, \tag{2.2}$$

where in this case, $g_m = f_m \cos \Phi_m$ is the distance from the principal focus to the field boundary (correcting for the finite length of the lens).

A small change to the ion mass $M = M_0\,(1 + \gamma)$ and to the velocity $v = v_0\,(1 + \beta)$

creates a displacement b''_m of the image according to

$$b''_m = r_m(\beta+\gamma)\left(1+\frac{f_m}{l'_m-g_m}\right)-b'_m\frac{f_m}{l'_m-g_m}, \tag{2.3}$$

where b'_m supposes that the displacement of the incident ion in the object plane could be non-zero.

2.2.2 Focusing in radial electrostatic fields

The treatment of radial electrostatic fields is similar to that in the homogeneous magnetic field case. We use similar naming of variables as Section 2.2.1, and we review and define these implicitly in Fig. 2.2. For the electrostatic field the image and object distance relation

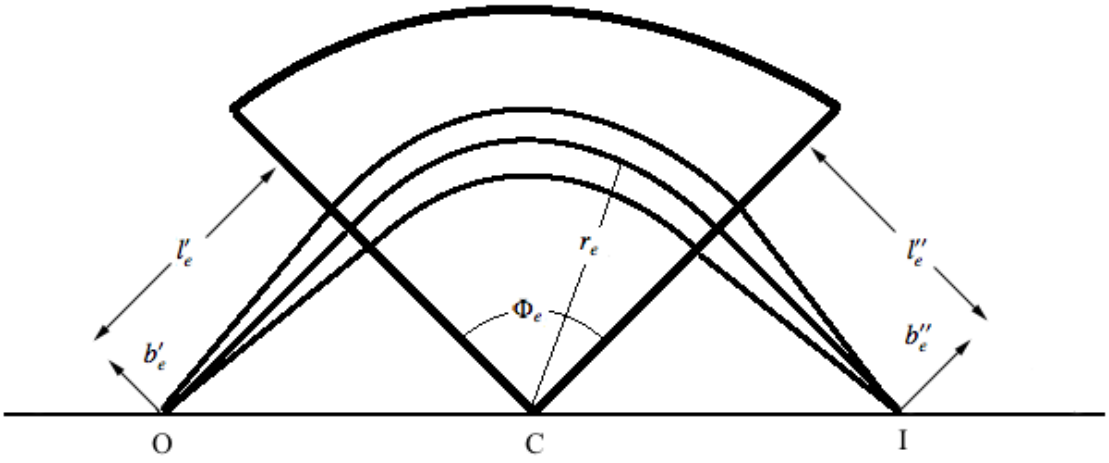

Figure 2.2: Focusing in a radial electrostatic field. For positively charged ions, the electric field lines point radially inward, converging on the point C. Ion trajectories and the relevant variables to describe them are defined in the figure, analogous to the discussion of Fig. 2.1 above.

is as usual given by

$$(l'_e-g_e)(l''_e-g_e)=f_e^2, \tag{2.4}$$

where the focal length f_e for this case is given by

$$f_e = \frac{r_e}{\sqrt{2}\sin\left(\sqrt{2}\Phi_e\right)}, \tag{2.5}$$

and where

$$g_e = f_e \cos\left(\sqrt{2}\Phi_e\right). \tag{2.6}$$

The image displacement for small velocity and mass variations, for the electrostatic case, is then given by:

$$b''_e = r_e\left(\beta + \frac{1}{2}\gamma\right)\left[1 + \left(\frac{f_e}{l'_e - g_e}\right)\right] - b'_e\left(\frac{f_e}{l'_e - g_e}\right) \tag{2.7}$$

where b'_e supposes a possible small displacement in the object plane.

2.2.3 Double focusing

Double focusing (i.e. focusing in both velocity and angle) may be achieved by using the image of a radial electrostatic analyzer as the object for the magnetic sector. In doing so, the velocity dispersion induced by the electrostatic region may be cancelled by the magnetic region. Care must also be taken to ensure effective directional focusing from the combination of lenses. In this scenario the final image displacement is:

$$b''_m = r_m(\beta + \gamma)\left(1 + \frac{f_m}{l'_m - g_m}\right) - \left(\frac{f_m}{l'_m - g_m}\right)\left[r_e\left(\beta + \frac{1}{2}\gamma\right)\left(1 + \frac{f_e}{l'_e - g_e}\right) - b'_e\left(\frac{f_e}{l'_e - g_e}\right)\right]. \tag{2.8}$$

Equation (2.8) already ensures angle focusing in the bend plane. Focusing in velocity would occur when the coefficients in front of the velocity variation β in Equation (2.8) total

zero, i.e. for

$$r_m \left[\frac{l'_m - g_m}{f_m} + 1 \right] - r_e \left[1 + \frac{f_e}{l'_e - g_e} \right] = 0. \tag{2.9}$$

While Manitoba II was designed based on this basic principle, the discussion above is a first order approximation in α (angular variation), β (velocity variation), and γ (mass variation), and is also valid only for normal incidence and homogeneous fields. We now provide a brief overview of the modifications to higher order, upon which Manitoba II's optics are truly based.

2.2.4 Higher-Order Ion optics and the Manitoba II mass spectrometer

A schematic diagram representing the Manitoba II spectrometer is shown in Fig. 2.3. In general, including both angular and velocity variations (α and β, respectively, as above), ions proceeding to the image plane of a combined electrostatic and magnetic analyzer system would arrive at a distance

$$b''_m = r_m \left(B_1\alpha + B_2\beta + B_{11}\alpha^2 + B_{12}\alpha\beta + B_{22}\beta^2 \right) \tag{2.10}$$

from the optic axis. The coefficients B_1, B_2, B_{11}, B_{12} and B_{22} all depend upon the geometry of the mass spectrometer, and the dependence was determined analytically in Ref. [28]. In order for double focusing to occur, all these coefficients must simultaneously equal zero. Several possible solutions are discussed in Ref. [28]. The most appropriate solution was selected for the design of the Manitoba II spectrometer.

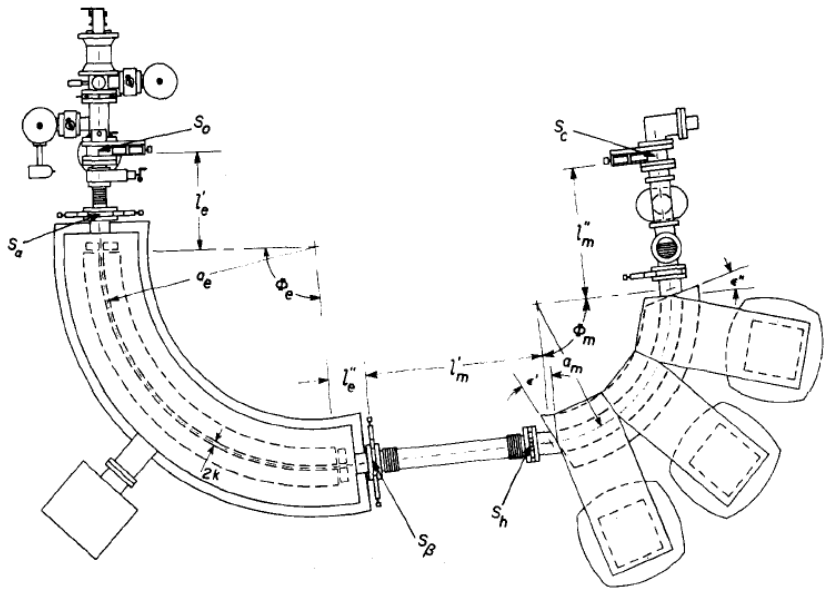

FIG. 1. Geometry of the mass spectrometer: $a_e = 100.00$ cm; $\Phi_e = 94.65°$; $a_m = 62.74$ cm; $\Phi_m = 90°$; $l'_e = 44.45$ cm; $l''_e = 17.63$ cm; $l'_m = 82.49$ cm; $l''_m = 59.46$ cm; $\epsilon' = 27°$; $\epsilon'' = 15°$; $2k = 2.000$ cm.

Figure 2.3: Geometry of the Manitoba II Mass Spectrometer (taken from Ref. [29] with permission). Ions emitted from the source slit S_0 are focused onto the image slit S_C. The ions are first analyzed by an electrostatic analyzer (shown on the left) and velocity dispersion is removed by the magnetic analyzer (on the right). Dimensional quantities analogous to those used in Sections 2.2.1 and 2.2.2 and Figs. 2.1 and 2.2 are defined on the diagram, and their values are presented in the included caption.

2.2.5 Median Path and Simple Mass Determination

A basic kinematic calculation for a particle moving along the median path of the magnet may be performed to allow for a simple prediction of the magnetic field required to see the various mass peaks. An ion of mass m and charge q moving with speed v in a magnetic field B oriented perpendicular to its direction of propagation will execute uniform circular motion according to:

$$F = qvB = \frac{\gamma m v^2}{r_m} \tag{2.11}$$

where r_m is the radius of the circle and $\gamma = 1/\sqrt{1 - v^2/c^2} \approx 1$ where c is the speed of light. The velocity of the ion may determined from the kinetic energy imparted to it by the acceleration potential V by inverting $qV = (\gamma - 1)mc^2 \approx \frac{1}{2}mv^2$. The radius of curvature of the path of the ion is fixed by the geometry of the spectrometer, and the magnetic field can be measured with an appropriately calibrated Hall probe. Therefore, solving Eqn. 2.11 for m allows a rough determination of the ion mass. Alternately, using the known masses and charges of relevant ions allows one to rapidly tune the spectrometer to find the appropriate magnetic field at which the desired species (e.g. protons) should be found. Solving Eqn. 2.11 for B and substituting for v using kinetic energy $T = mv^2/2$, yields:

$$B = \frac{\sqrt{2Tm}}{qR} \tag{2.12}$$

Eqn. 2.12 allows for calculation of the magnetic field using convenient values determined from the various accelerator settings.

It is worthwhile noting that the electrostatic analyzer (ESA) portion of the mass spectrometer need not be adjusted when scanning the magnetic sector through various magnetic field values to search for various ionic species. This effect arises because the ESA supplies

an electric force that is centripetal, so that:

$$qE = \gamma m v^2 / R \approx 2T / r_e \tag{2.13}$$

where r_e is the radius of the ESA. Therefore selecting the ESA potential difference, by applying positive and negative voltages to outer and inner plates, selects the electric field strength E along the median path, which in turn selects the particle's *kinetic energy*, which has already been selected by the acceleration potential. The ESA setting should therefore be essentially the same for all ionic species accelerated from the ion source. It is therefore sufficient when tuning the accelerator to adopt the following stepwise procedure:

1. Select the acceleration potential desired for the silicon detector tests.

2. Scan the ESA voltage difference to achieve maximum transmission through the ESA.

3. Scan the magnetic spectrometer to select the ions of interest (in this case, protons).

Of course it is also wise to iterate tuning the ESA and magnetic spectrometer to ensure maximum transmission in practice. Usually this was done for the ions of interest (protons) and then the ESA parameters would be fixed when scanning the magnetic spectrometer to search for other ionic species of lesser interest (H_2^+, etc.) in the beam.

2.3 Silicon detectors

A brief overview of silicon detector attributes and function are provided in this section. The discussion is based primarily on Refs. [30] and [31].

2.3.1 Semiconductor properties

Silicon detectors are a form of semiconductor diode detector. Such detectors rely on the creation of electron-hole pairs within the medium which are then collected on external electrodes.

The classification of a material as a semiconductor is determined by the band structure for the material. The energy levels available to electrons in crystalline materials exist as energy bands. Fig. 2.4 shows a schematic diagram of the energy band structure for insulators semiconductors and conductors.

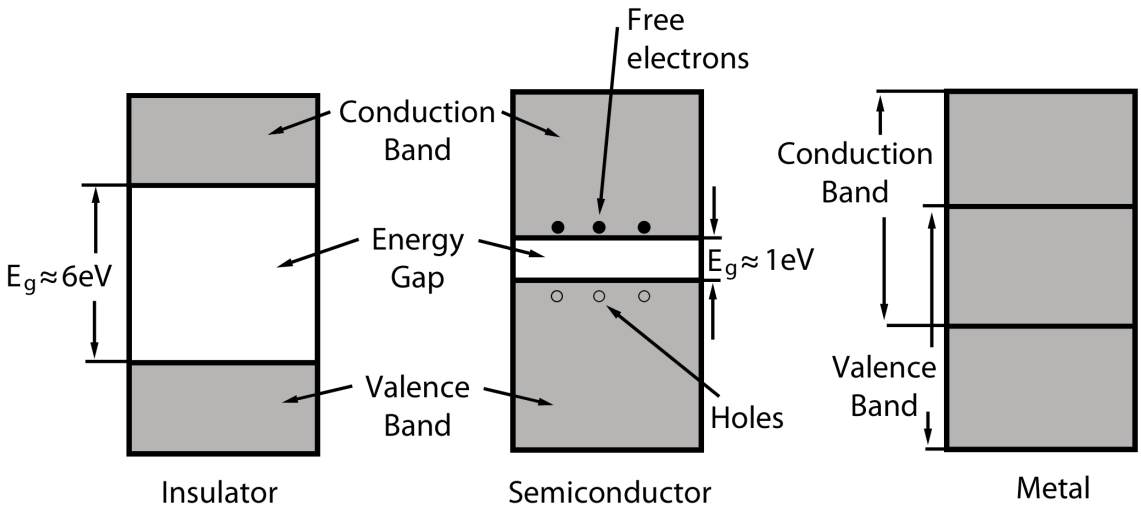

Figure 2.4: The band structure for an insulator, a semi-conductor and a conductor (after Ref. [30]).

Energy bands consist of many closely spaced discrete levels which are so similar that they can be considered to be a continuum of energy levels. As shown in Fig. 2.4, there are generally two bands of interest when characterizing the electrical properties of a material, the valence band and the conduction band.

Electrons in the valence band are bound to their associated atom. At the low temper-

ature limit ($T = 0$ K), all electrons would be confined to this band. For $T > 0$, electrons can be thermally excited into the conduction band. These electrons are then able to move throughout the entire crystal structure giving rise to currents. The separation between the valence band and the conduction band is called the band gap.

As shown schematically in Fig. 2.4, for metals, the band gap is zero and so electrons can be exited into the conduction band with very little thermal excitation energy providing little resistance to current flow. For insulators, the band gap is $\gtrsim 5$ eV so that thermal energy does not typically excite electrons into the conduction band, and the resistance to current flow is large. For semiconductors, the band gap is ~ 1 eV so that thermal energy can excite some electrons into the conduction band so that current may also flow.

In semiconductors, charge may be carried by either electrons or holes. A hole is formed in the valence band when an electron from the valence band is excited into the conduction band. Such a hole can then be filled by a neighboring atom's valence electron allowing the hole to move to that atom. Holes in the valence band therefore act as positive charge carriers, while electrons in the conduction band electrons are the negative charge carriers. This form of conduction using both holes and electrons is different from the conduction in metals where only electrons conduct charge.

For the case of a pure semiconductor, there are an equal number of holes and electrons in the conduction band. The relative numbers of holes and electrons available for conduction can be altered by doping the semiconductor with other materials.

When the dopant is an electron donor, each dopant atom adds an electron which does not fit in the valence band. In silicon the energy level for this extra electron may be only 0.05 eV less than the minimum conduction band energy. This extra electron can therefore easily be thermally excited into the conduction band thus enhancing the conductivity of the semiconductor. As well these extra electrons can drop down and fill existing holes in the

valence band thus reducing the number of holes. Such semiconductors have electrons as their primary charge carriers and holes as their minority charge carriers and are known as n-type semiconductors.

The alternate doping scenario occurs when the dopant accepts electrons from the valence band. Such an acceptor dopant results in an excess of holes in the semiconductor. The introduction of an acceptor dopant creates an additional energy level just above the valence band energy, electrons excited into this new level leave behind additional holes and reduce the number of electrons in the conduction band. Materials doped with an acceptor material have holes as their primary charge carriers and electrons as their minority carriers and are called p-type semiconductors.

Some common donor dopants are arsenic, phosphorus and antimony. These are used for n-type semiconductors, whereas p-type semiconductors are usually doped with gallium, boron and indium acceptor atoms. Generally the amount of dopant used is very small, typically 10^{13} atoms/cm^3. This value can be compared to the number atomic density of crystalline silicon which is 10^{20} atoms/cm^3. There are however cases where heavily doped semiconductors are used; one relevant purpose is to form electrical contacts with semiconductor detectors.

2.3.2 Silicon as a detector of ionizing radiation

Silicon detectors are created by forming a junction between n-type and p-type materials. For simplicity consider a piece of n-type and p-type material joined together to form a junction as shown in Fig. 2.5. At the interface between n-type and p-type materials exists a zone in which the extra electrons from the n-type material diffuse into the p-type and holes from the p-type diffuse into the n-type. Initially, each material is charge neutral,

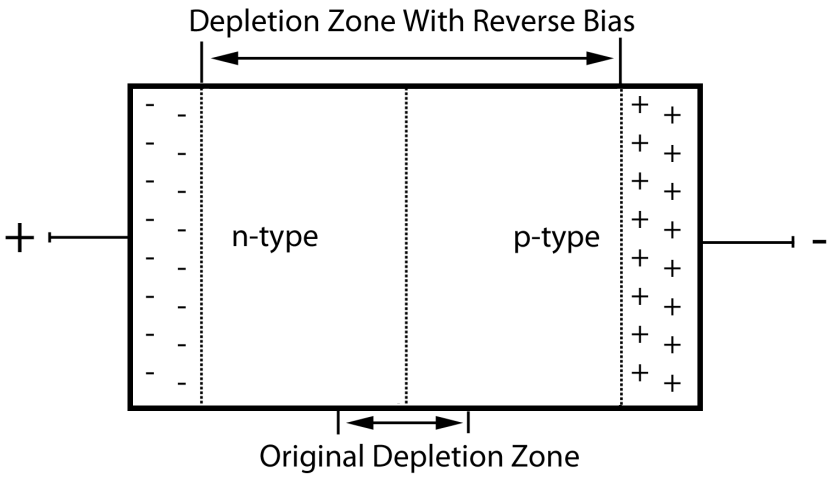

Figure 2.5: The depletion zone in a reverse biased junction.

so the diffusion causes a net negative charge on the p-type side and a net positive charge on the n-type side. The charge buildup induces an electric field which is responsible for establishing an equilibrium state in which further net diffusion is halted. The resultant voltage difference is named the contact potential and generally it is $\sim$ 1 V. The region in which there are no mobile charge carriers between the regions of built up charge is known as the depletion zone. Any charge carriers which enter or are created in the depletion zone are forced to leave by the electric field. This effect is the basis for the use of silicon as a detector; ionizing radiation which enters the depletion zone can create electron-hole pairs which then form a current which can be measured if electrical contacts are made on each side of the junction.

The depletion zone can be enlarged by applying a reverse bias to the junction, e.g. by applying a positive voltage to the n-type side and grounding the p-type side. The effect of a reverse bias voltage is to draw the electrons and holes away from the junction, thus widening the depletion zone size, as shown schematically in Fig. 2.5. The increase in the

depletion zone causes the active detection volume for the detector to increase. The reverse bias voltage is limited since at some applied voltage the detector junction breaks down and starts conducting.

2.3.3 Large Area Silicon Detectors

In a neutron beta decay experiment where both the protons and electrons are detected, the detector needs to detect as large as possible a range of electron energies (typically $50-782$ keV), as well as the 30 keV protons. The detector must therefore be simultaneously thick enough to stop high-energy electrons, while having a thin enough entrance window to admit the low-energy protons.

Silicon detectors offer a combination of good timing ($\lesssim$ns), and good energy resolution ($\sim$keV), with high detection efficiency, and stability. For larger detectors, thermal noise in both the detector and the associated electronics can dominate the noise performance of the detector. When cooled to $\sim LN_2$ temperatures, the noise performance of silicon detectors can improve. The cooling of the detectors causes a decrease in the number of charge carriers by reducing the thermal energy available to excite electrons into the conduction band. As a result, there is less leakage current through the reverse-biased pn-junction, thereby reducing the detector noise.

Prototype detectors for the Nab experiment are shown in Fig. 2.6. The detectors were fabricated by Micron Semiconductor Ltd. [32]. The detectors are segmented to provide position sensitivity. They have been fabricated to be as large area as possible, so as to provide a large edge-free fiducial area viewing the decay region of the spectrometer. They are fabricated from a monolithic disk of silicon 6" in diameter cut from a high-resisitivity ingot of silicon. High-concentration doping for the contact electrodes is done by ion implantation,

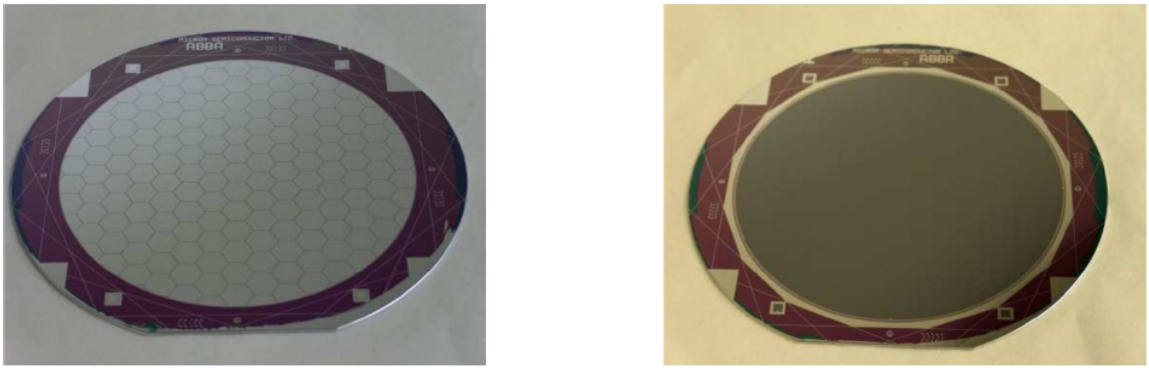

Figure 2.6: Prototype detector for the Nab experiment [22].

as is usual for these detectors.

The thickness of the detectors is 2 mm in order to stop the highest energy electrons at normal incidence. The front of the detector is treated specially, presenting a very thin dead layer to incident particles. The dead layer consists of a thin p-type implant with a thickness of a mere 100 nm covered by a thinner layer of Al. The large 100 cm^2 active area is segmented into 127 separate hexagonal pad regions. Each pad has a high-gain preamplifier located immediately behind it. The entire setup is mounted to a cold finger which is cooled to LN_2 temperature (77 K). Signals from the detector are fed to a fast data acquisition system consisting of waveform digitizers.

The initial application of our proton accelerator will be to test these large area silicon detectors. Key questions on the efficiency for proton detection of each pad will be addressed by scanning either the proton beam or by moving the detectors themselves.

Chapter 3

Apparatus

3.1 Overview

The proton accelerator system was created by modifying the existing Manitoba II mass spectrometer (see Fig. 3.1) with a new ion source and detector region. A detailed description of the Manitoba II mass spectrometer may be found in Ref. [29]. The principal modifications to the basic setup were:

- A new proton source based on the Penning ion generator concept was constructed, along with an associated new gas handling system for the source.

- A new high voltage accelerating supply capable of supplying 50 keV was installed. With the present acceleration tube, this allowed an accelerating potential of $\gtrsim$ 30 keV to be achieved.

- A detector region was designed and constructed to house the proton detectors, with its own vacuum system based on a turbomolecular pump. This system could be vented when required using a gate valve. Both a chevron-style microchannel plate

(MCP) array and smaller test silicon detectors were housed in this detector region.

We now describe the overall apparatus, with somewhat more focus on the new systems identified above.

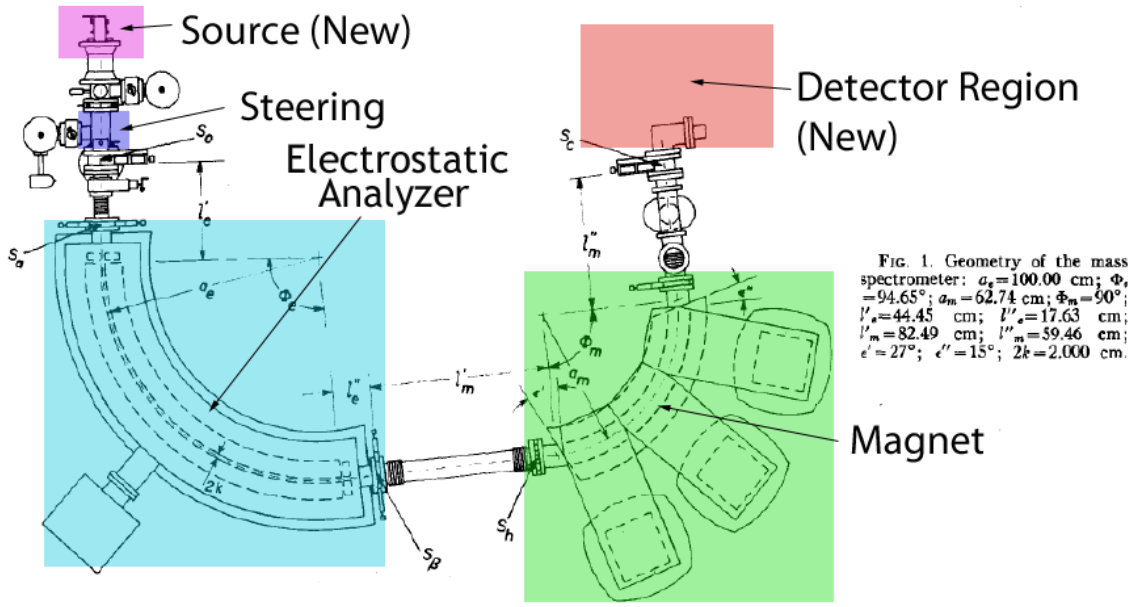

Figure 3.1: Overview of the proton accelerator, note the new source and detector regions which are modified from those in this schematic

3.2 Ion Source

The ion source was based on a the Penning ion generator (PIG) source described in Ref. [26]. This style of source was chosen for its simplicity of design; there is no filament and beam current can be controlled using the arc voltage or the gas flow. The PIG source in principle also allows the generation of stable current of protons, as long as the source parameters are controlled properly. We generally found this also to be true in practice; over the course of the day, the source would require very little attention, and the current was stable.

The principle behind the source is to create a small chamber filled with the desired gas then apply a voltage from the anode to the cathode which will continuously discharge in a controlled fashion, generating a plasma. Magnets are used in the source region to increase the path length that the free ionizing electrons traverse inside the source thus maintaining the plasma.

Our source is shown schematically in Fig. 3.2. To simplify source construction an existing ion source from the Manitoba II mass spectrometer was used as a starting point and modified. This provided a useful housing for the ion source, which readily fit into the Manitoba II system. The main modifications were to attach two floating anode feedthroughs and a floating gas feedthrough; the housing itself is the cathode. Inside the source cavity the anode feedthroughs hold an anode ring in place isolated from the cathode walls. Also 1/4" neodymium magnets [33] were stacked in the center of the cavity to provide a magnetic field in the source region. The source cavity was enclosed by a faceplate which has a hole in the center to provide the ions for the beam. When attached to the mass spectrometer it was isolated electrically by a glass cylinder, which was used as an acceleration tube.

3.2.1 Gas supply

The gas supply system is shown in Fig. 3.3. The main reservoir is a small gas cylinder which can be closed to the rest of the system. This allows for the same gas mixture to be stored for longer periods of time, without worrying about the small leaks the overall system has to the atmosphere.

Operation of the ion source required the use of an argon/hydrogen gas mixture. It was found that a mixture of equal partial pressures of hydrogen and argon, as measured by a spring-type pressure gauge connected to the manifold, provided an effective plasma for the

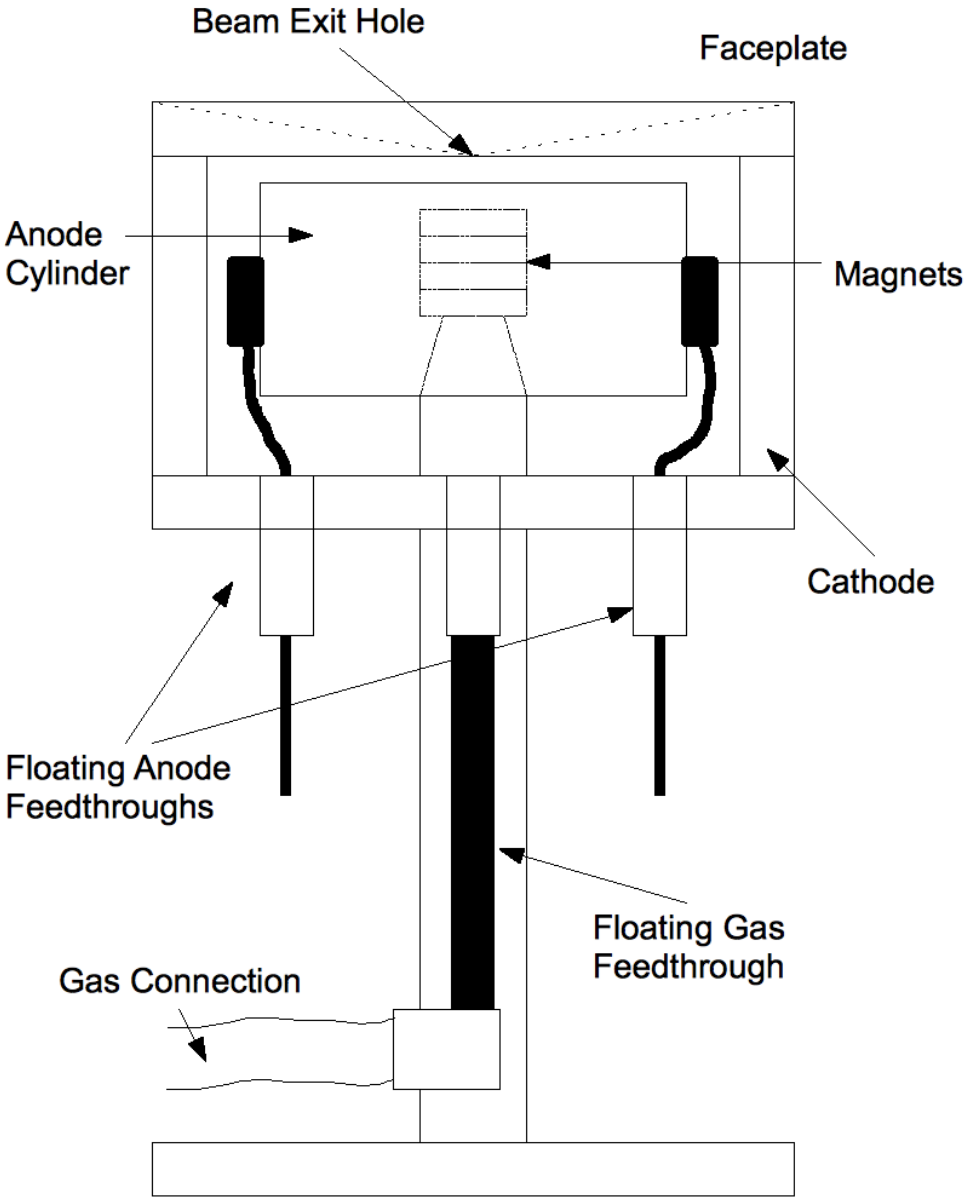

Figure 3.2: A schematic diagram of our ion source. Gas is supplied from a reservoir (see Fig. 3.3) to the floating gas connection through a manual needle valve. The arc voltage is applied to the external cathode by an alligator clip connection and the anode voltage is connected to the anode by a floating anode feedthrough. Magnets are mounted and held in place by their field inside the anode region. A faceplate mounted by screws to the source provides a small hole through which ions are accelerated into the mass spectrometer region.

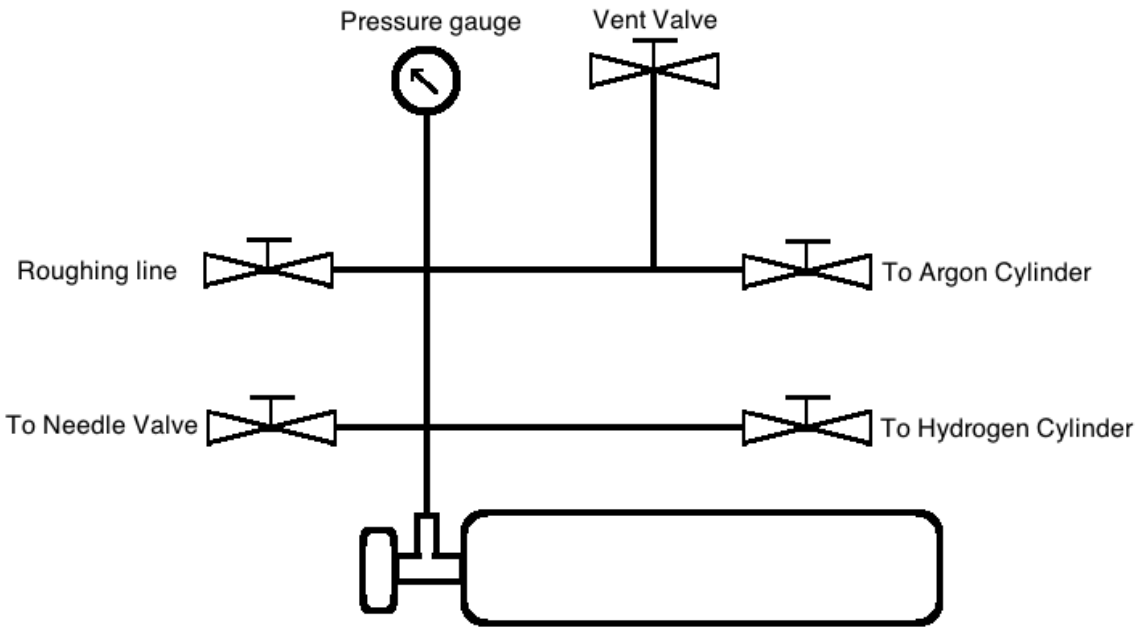

Figure 3.3: The ion source gas supply consists of a reservoir (bottle) which is connected by valves to: a roughing line for evacuation, argon and hydrogen cylinders for gas filling, a gauge to measure the pressure, a vent valve for bringing the reservoir to atmosphere and a line to the needle valve which supplies the ion source with gas.

source. This mixture was created in the gas reservoir using hydrogen and argon cylinders to fill the system after evacuation to ~ 50 mTorr using a roughing pump. A needle valve was located between the gas reservoir system and the source to provide an appropriate gas flow to the source region.

3.2.2 Source Vacuum Connections

A schematic diagram of the source region vacuum system is provided in Fig. 3.4. The

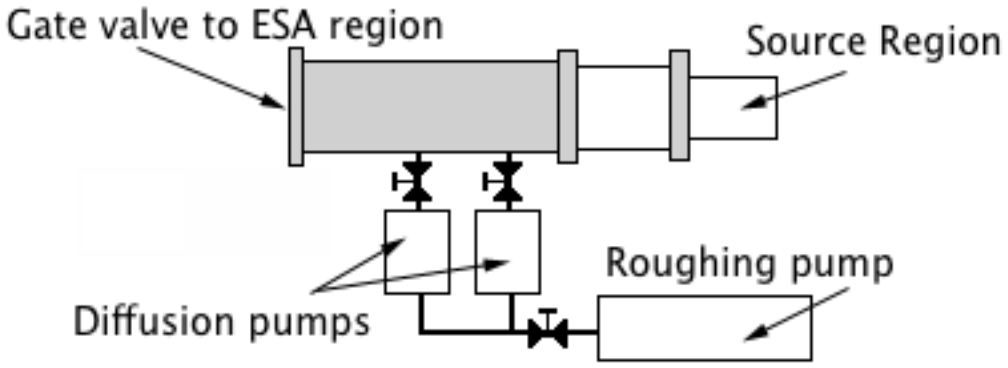

Figure 3.4: The source region is pumped by two diffusion pumps (with LN_2 cold traps) which can be closed off to the source region by two gate valves. The diffusion pumps are backed by a single rotary pump. A gate valve can be used to isolate the source region from the rest of the mass spectrometer. A needle valve attached to the ion source provides the gas flow required to generate a plasma and a vent valve allows for the source region to be brought up to atmosphere.

pressure in the source could be monitored by either an ion gauge in front of a diffusion pump, or less directly via the backing pressure for the diffusion pumps which pump the source region. We alternately use these two methods of reporting source pressures in this thesis.

3.2.3 Typical Source Operation Parameters

The plasma could be maintained with a anode cathode voltage difference of typically 400 V. The voltage and needle valve could be adjusted to provide a steady arc current of $\sim 1 - 4$ mA.

3.3 Manitoba II mass spectrometer

We provide a basic discussion of the spectrometer. We refer the reader also to Fig. 2.3 which contains a schematic diagram of the geometry of the spectrometer.

3.3.1 Electrostatic analyzer (ESA)

The electrostatic analyzer (ESA) portion of the Manitoba II mass spectrometer permits velocity focusing for the double focusing spectrometer. Ions leaving the ion source are accelerated by a potential difference which defines their energy. The ions are then brought to a focus at the object slit by the use of vertical and horizontal deflection plates and then a quadrupole magnet.

The ions that pass through the object slit then travel into a radial electric field defined by the voltages applied to inner and outer ESA plates. The plates are gold plated electrodes separated by a distance of 2 cm and arranged to to define the circular ion path desired. The electric field supplies the force which causes the ions to move in a circular path toward the object slit. Ions exiting from the object slit have a well-defined energy and continue onward to the magnetic spectrometer. Vacuum in the ESA region is supplied by a turbomolecular pump and an ion pump, and is maintained at the 10^{-7} Torr level as read from the Ion pump controller. Typically, for 30 keV protons, the ESA voltages are set at 618.62 V and

-618.62 V resulting in a potential difference of 1237.24 V between the plates. The voltages are supplied by two separate power supply channels.

3.3.2 Magnetic Spectrometer

The ions that have passed through the ESA travel a distance of 82.49 cm before entering the sector magnet used as a magnetic spectrometer. The magnetic sector is kept to a vacuum of 10^{-8} Torr by an ion pump located just after the magnet in the beamline. The magnet consists of three main sectors which are each made up of four coils, each coil consisting of sixty turns of copper wire. The magnet power supply is a 200 A Bruker (B-MN15/200) supply. Water cooling is supplied to both the power supply and the magnet coils. The sector has a magnetic radius r_m = 62.74 cm and diverts ions from entrance to exit through an angle $\Phi_m = 90°$.

3.4 Detector Region

The detector region consists of an 8" Conflat (CF) cross attached to the end of the Manitoba II mass spectrometer and isolated by an 8" CF gate valve. The gate valve is attached to a custom machined adapter flange which converts an indium seal flange on the exit of the spectrometer to 8" CF, indium seals being used for most flanges in the Manitoba II system. The adaptation to CF makes connection to a variety of equipment possible.

Figure 3.5 depicts the detector region, whose main chamber is a four-way 8" CF cross. Mounted to the top flange of the cross was a linear motion feedthrough and electrical feedthroughs for the MCP detector. The back flange has a BNC type feedthrough which was used to mount a small silicon detector. The detector region could be isolated from the mass spectrometer by a gate valve, for easy access to the detectors. The region possessed

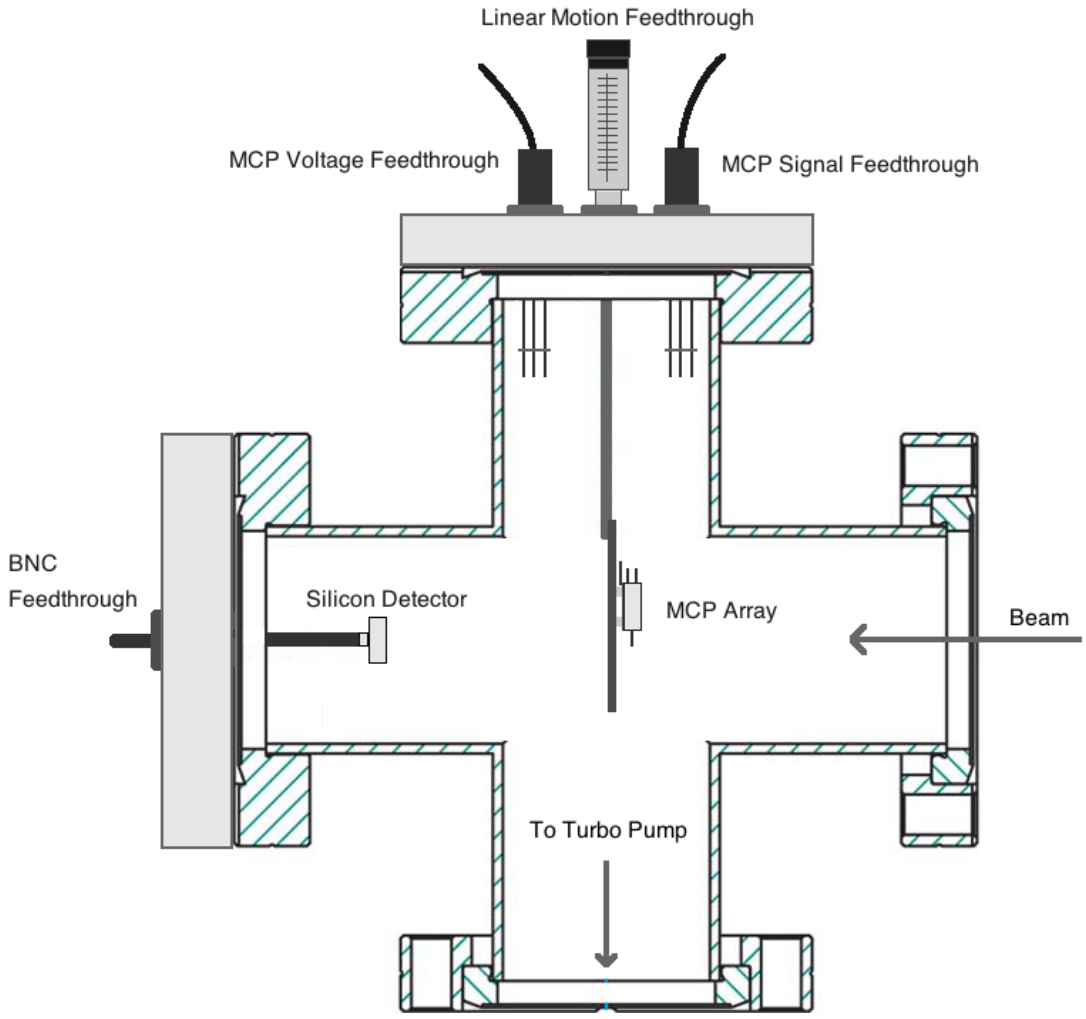

Figure 3.5: The detector region consists of an 8" Conflat cross mounted on a gate valve after the magnet. The top flange of the cross has five 1.33" CF holes inscribed upon it. These were use to mount two electrical feedthroughs for output signal and operational voltages, a linear motion feedthrough, and an ion gauge. The linear motion feedthrough controlled the location of the MCP detector holder. The back flange had its own centered 1.33" CF feedthrough upon which was mounted a BNC feedthrough, and on the BNC feedthrough a test silicon detector was mounted. The detector region was pumped by a turbomolecular pump located on the bottom flange of the cross.

Feedthrough Reading (mm)	Description of setting
20	Minimum feedthrough setting
39.5	Hole in mounting plate is centered in cross
77.5	MCP detector is centered in cross
130	Maximum feedthrough setting

Table 3.1: Important feedthrough settings.

its own vacuum system, consisting of a turbomolecular pump backed by a roughing pump. The vacuum in the region was maintained at typically 10^{-9} Torr. This value would increase to about 10^{-8} Torr upon opening the gate valve connecting the detector region to the magnet and ESA vacuum region.

3.5 Microchannel plate (MCP) detector array

The first detector array used to detect protons consisted of two microchannel plates (MCP's) arranged in a chevron formation and mounted on a support arm shown in Fig. 3.7. The location of the MCP center relative to the inside of the top flange of the cross is given in table 3.1. These values are calculated using the designer specifications for flange thickness (0.88 in) and feedthrough location (unextended location of the end of the feedthrough arm is 3.18 in). The minimum feedthrough region was decided based upon observing the wires connected to the MCPs when moving the support arm, the minimum setting was to chosen to minimize the bending of the wire connections to the MCP array. The centering of the hole in the support arm mounting plate is important to allow the beam to continue on to the silicon detector further downstream. The MCP centered setting is important for making measurements with the MCP detectors. Finally the maximum setting is the point at which the wires are reaching the end of their extended lengths.

We provide here a brief review of the function of MCP detectors. A schematic diagram

of an MCP is presented in Fig. 3.6. MCP's consist of a circular surface area with thousands

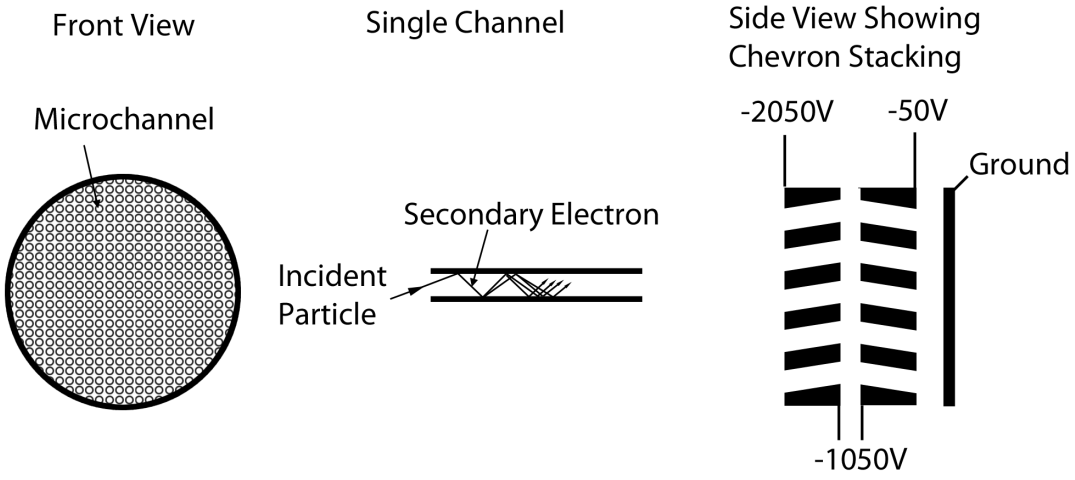

Figure 3.6: Microchannel plate (MCP) operational schematic diagram. Left: an individual plate. Middle: electron multiplication in a single channel. Right: chevron arrangement of two MCPs.

of tiny channels. When a particle (in this case an ion) strikes one of the channels, secondary electrons are liberated which initiate a cascade of secondary electrons that are multiplied by further collisions within the walls of the channel. An applied voltage difference (of typically kV) across each plate accelerates the electrons towards the collection plate located behind the MCPs themselves.

In our case, two MCP's in a chevron arrangement were used, similar to the right side of Fig. 3.6. Our collection plate is connected to a signal wire which is terminated by a 50 Ω resistor, across which a voltage pulse is measured by our data acquisition (DAQ) system. The MCP's were mounted within a specially designed holder, which is displayed in Fig. 3.7. High voltage and signal wires were connected via feedthroughs in the top flange using copper wire encased with insulating beads. A high voltage (~ -1.8 kV) was provided to a voltage divider located in an external aluminum box, which provided the voltages for

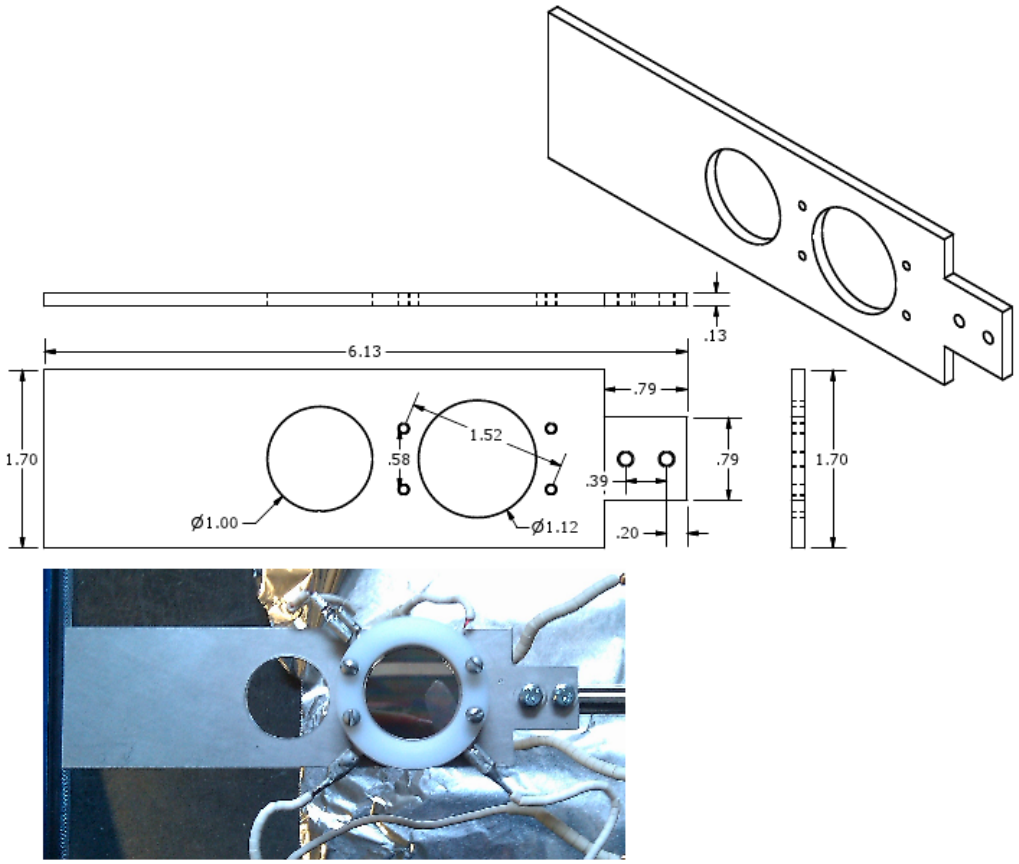

Figure 3.7: MCP Support Arm schematic and picture with MCP array mounted

the front and back of the two MCP stages. The signal was transferred by a BNC type cable from the flange vacuum feedthrough to the DAQ system.

The MCP's were manufactured by Photonis [34]. Each plate provided a gain of $\sim 10^4$ while drawing a current of 21.4 μA read from the power supply during operation. Each plate has a quality diameter of 25 mm defining the fiducial area. Each microchannel is nominally 10 μm in diameter, with a length to diameter ratio of 40:1, a bias angle of 12°, an open area of 64% and a thickness of 0.43 mm.

3.6 Silicon Detector

For this experiment Ortec ULTRA (ion implanted) detectors (part number CU-012-100-300) were used to search for $\sim$ 30 keV protons. A picture of one of these detectors mounted on its BNC feedthrough on a 1.33" CF flange is shown in Fig. 3.8.

The silicon detectors have a depletion depth of 300 μm and an active area of 100 mm^2. They are operated with a positive bias voltage of 100 V. The dead layer for these detectors is dominated by a region of $\sim$ 50 nm boron-implanted silicon, according to the manufacturer's specifications.

3.6.1 Silicon dead layer transmission

A calculation was made of the proton transmission through the silicon dead layer for the ORTEC silicon detectors used. The dead layer for the ion implanted silicon detectors is created by the inactive ion implanted surface region which provided the electrical contact properties to the entrance window. Ortec provides a dead layer value of approximately 50 nm silicon equivalent.

The mean range for 30 keV protons in silicon was found using the PSTAR database

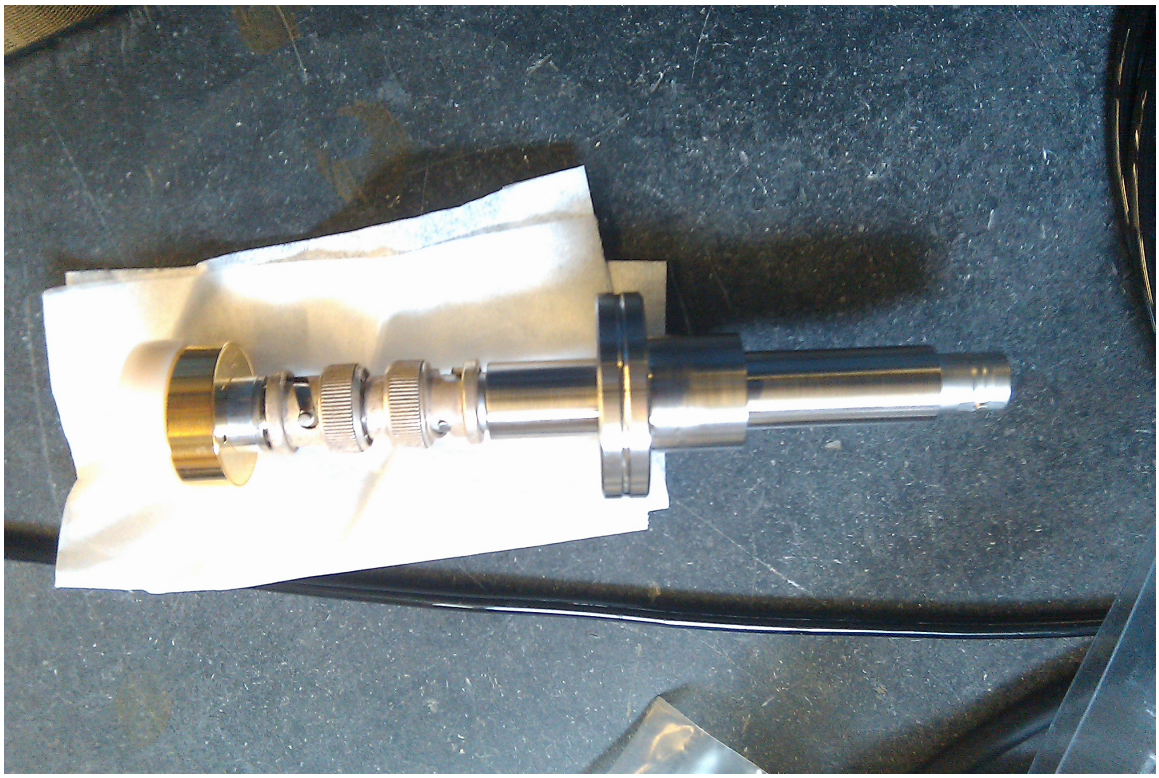

Figure 3.8: Ortec model CU-012-100-300 silicon detector mounted on a 1.33” CF BNC feedthrough.

[35]. The range from PSTAR was 7.0×10^{-5} g/cm^2. The density of silicon is ρ = 2.33 g/cm^3. Therefore the range of a 30 keV proton in silicon is 300 nm, which is 250 nm beyond the dead layer of these detectors.

The mean energy loss (stopping power) of a 30 keV proton from the PSTAR database is 5.0×10^2 MeV·cm^2/g, or 1.2 keV/(10 nm). For a 50 nm dead layer, this would correspond to an energy loss of $\sim$ 6 keV. Since the energy loss is in a region where it is somewhat dropping as the energy decreases (according to the PSTAR tables), an estimate of $5-6$ keV energy loss is reasonable. The detectable energy in the detector is therefore expected to be $24-25$ keV for a 30 keV incident proton.

It is therefore important to ensure that the best possible noise conditions exist when attempting to detect the protons.

Chapter 4

Method and Results

4.1 Gas Parameters

We begin with a general overview of accelerator operation to provide context for the experimental results (for additional details on typical operating parameters and trouble shooting see Appendix A). The source uses a 1:1 Ar:H_2 gas mixture which is leaked into the source through a needle valve. The exactness of the 1:1 ratio is approximate since only rough pressure gauge readings were used to determine the ratio. The pressure and cleanliness of the source region was very important to effective operation. Problems with arcing due to the acceleration potential were found to correlate with the quality of the source vacuum prior to the introduction of gas. During operation, the pressure at the entrance to the diffusion pumps as read by an ion gauge was typically 10^{-5} Torr. This pressure is referred to throughout this chapter as the source pressure. The exact pressure in each measurement was decided based on the generation of a stable arc current in the source. The characteristics of the various source operating parameters are discussed further in Section 4.6.

4.2 Magnet Calibration

The magnetic field control program entitled "BORIS" provided a magnetic field reading in units of μV based upon a Hall probe located inside the magnet. Calibration of the Hall probe was required in order to determine the field value in the more useful units of Gauss. To calibrate the Hall probe a reference Hall probe calibrated in kG was inserted next to the existing Hall probe and measurements for various field values were recorded. The results of the calibration are presented in Fig. 4.1. The result of a best fit to a straight line for the

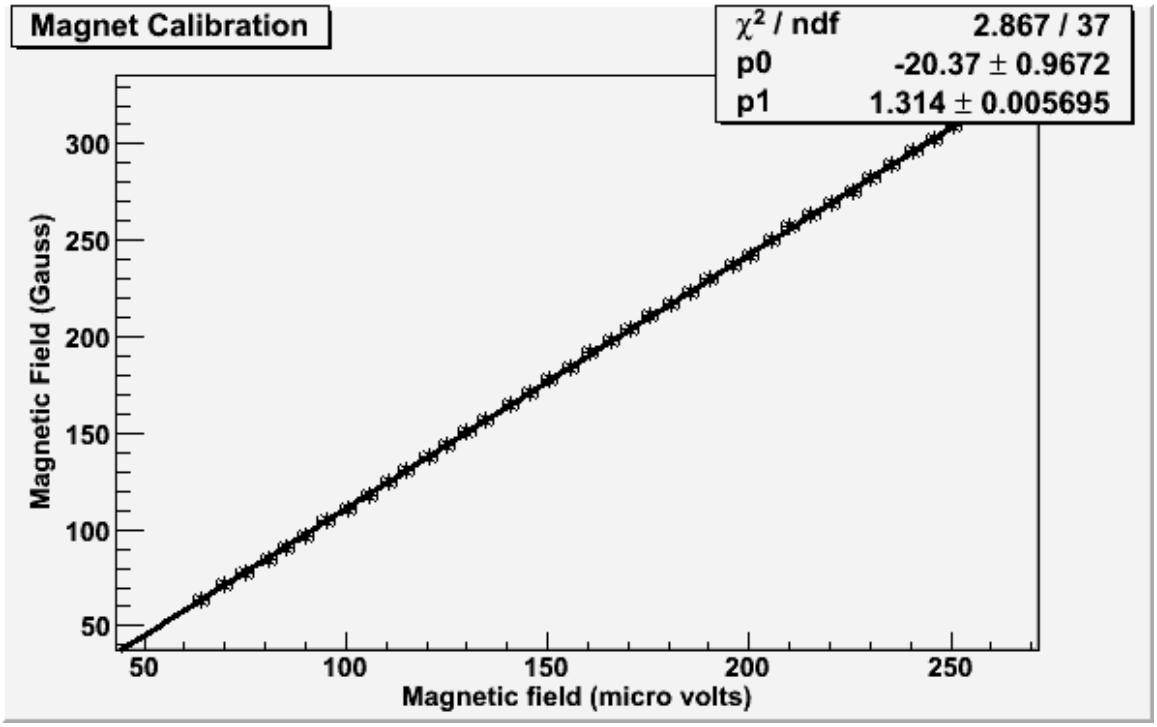

Figure 4.1: Plot of magnetic field in Gauss vs magnetic field in μV for the purposes of hall probe calibration

data is:

$$B(\mathrm{G}) = 1.314 \times V(\mu\mathrm{V}) - 20.37 \tag{4.1}$$

where V is the Hall voltage read in μV and B is the magnetic field in Gauss. As shall be seen from calibration with known ions, this form of calibration against a Hall probe was found to be good to the percent level.

4.3 Data Acquisition

Data acquisition for the microchannel plates was performed using several VME (Versa Module Eurocard) modules driven by the MIDAS (Maximum Integrated Data Acquisition System) software [36].

The system consisted of a CAEN [37] Universal multichannel power supply system (model SY2527 LC), which provided the output voltage for both the ESA and for the microchannel plates. The output signal from the microchannel plates was amplified by a variable gain fast amplifier (CAEN model V974). The amplified signal was passed to a quad linear fan in-fan out (CAEN model V925) used as a leading-edge discriminator. Rates were determined by counting the number of gate signals provided by the discriminator to the gate input of a peak-sensing analog to digital converter (ADC) (CAEN model V1785N). The VME modules were housed in a WME 8010 CAMAC crate. Communications with the modules occurred via fiber optic link with a computer through a CONET-VME bridge (CAEN model V2718 VME-PCI). The custom portions of MIDAS system code were provided by P. Wang. Data from the MIDAS system were converted to ROOT format by the MIDAS analyzer, which could subsequently be analyzed in ROOT [38]. With this setup a wide variety of measurements are possible, however for the purpose of this thesis counting the gates which corresponded to micro channel plate output signals were the only measurements performed.

4.4 Kinematic Calculations and Test of Field Calibration

The equations from Section 2.2.5 can be used to calculate an expected location for a peak in terms of the magnetic field value. This expected location can be compared to the experimentally observed peaks to test the calibration of the magnet and also to give confidence in the ability to correctly identify the proton peak.

The magnetic field can be determined using Eqn. 2.12 , repeated here for convenience:

$$B = \frac{\sqrt{2Tm}}{qR} \tag{4.2}$$

with the appropriate values from Section 2.2.5 the magnetic field values for various ion peaks can be calculated, the following calculation is for the proton peak with an accelerating voltage setting of 27245 V:

$$m_{proton} = 938.27 \frac{\text{MeV}}{c^2} = 1.602 \times 10^{-27} \text{ kg} \tag{4.3}$$

$$T = 27245 \text{ eV} \tag{4.4}$$

$$q = 1.602 \times 10^{-19} \text{ C} \tag{4.5}$$

$$R = 0.6274 \text{ m} \tag{4.6}$$

$$B = 0.03802 \text{ T} = 380.2 \text{ G.} \tag{4.7}$$

Observations of the various peaks were made by manually sweeping the current in the magnet and observing the MCP count rate. Whenever a rise in the MCP signal was detected, the reading on the Hall probe was noted. In this way the various peaks in the proton region were found.

Table 4.1 shows the experimental peak locations, and the calculated locations for various ions using only the acceleration voltage for to determine kinetic energy (T) (calculated

using equation (4.2) above). The solid vertical lines in the various plots throughout this chapter are calculated using only the HV value and the dotted lines are calculated using the HV value with the addition of the arc voltage value. The two calculated values should provide a sense of the energy spread due to ions being produced at various locations in the source. The same HV setting (27245 V) was used for all values in the table below.

Table 4.1: Table of calculated (based on equation (4.2)) and experimental peak locations, expressed in terms of magnetic field in the spectrometer magnet. The masses for the various ions were taken from Ref. [39]. A peak at the energy $H_2^+/2$ is expected because of dissociation of H_2^+, as described in the text.

HV (V)	Ion Species	Atomic Mass (u)	Experimental Value (G)	Calculated Value (G)
27425/2	$H_2^+/2$	1.00739	268.7	268.8
27425	H^+	1.00739	380.4	380.2
27425	H_2^+	2.01533	538.1	537.8
27425	H_3^+	3.02327	656.3	658.5

As seen in Refs. [24, 25], a peak was expected at half the value of the magnetic field of H_2^+ peak. This peak results from dissociation of the H_2^+ ion prior to entering the magnetic spectrometer. The H_2^+ ion dissociates into a H^+ and a H atom which share the kinetic energy of the initial H_2^+ ion. Upon dissociation the H^+ ion and a H atom continue through the spectrometer giving rise to the peak labelled as the H_2^+ dissociation peak. The calculated peak locations for the various species are in agreement to within a fraction of a percent, indicating both the validity of the identification of the species, and the calibration of the spectrometer.

4.5 Magnet spectra

Magnet spectra (count rates in the MCP as a function of the magnetic field) were acquired by changing the magnetic field by fixed increments and counting at each field setting, regardless of whether a peak was being sensed. These spectra were obtained as a means to search for any unknown peaks or possible beam-related backgrounds which might have an impact on the proton beam. In addition, once the peaks had been located using the broad spectrum scan, finer scans over the individual peaks were performed. As well, spectra were acquired for different acceleration voltages.

During acquisition of a magnet spectrum, the acceleration voltage, ESA voltages, source pressure, source arc voltage and all other focusing parameters were held constant. The settings of these parameters would have been selected by manually maximizing the MCP counts for the proton peak. Once the appropriate settings were established, the magnetic field was set to a small value, well below any peaks of interest, and a scan was begun. In the scan, the magnetic field was incremented by a fixed step size, and counts in the MCP would be acquired for a fixed amount of time at that field setting. The field would be incremented until its value lay beyond the field setting for the H_3^+ peak.

There are two units available for magnetic field adjustment, one is the output of a Hall probe which is located within the magnet, the other is the output of the Bruker power supply (referred to as "Bruker units", which correspond to a DAC setting within the power supply, where the analog output of the DAC is proportional to current). The use of the Bruker units is only valid when one moves consistently in one field direction change since the field is affected by magnetic hysteresis from the magnet's iron core.

The advantage of using Bruker units over Hall probe readings is that considerably finer control over the magnet setting can be gained. However, due to hysteresis, the field value

corresponding to each Bruker setting varies. Thus the Hall probe was also always recorded for each measurement despite its worse resolution. The Hall probe reading was limited to about 1 Gauss in stability over time and reproducibility.

A spectrum obtained using an acceleration voltage of 27245 V is shown in Fig. 4.2. For this spectrum, the source arc voltage was 410 V, the source arc current was 4 mA, and

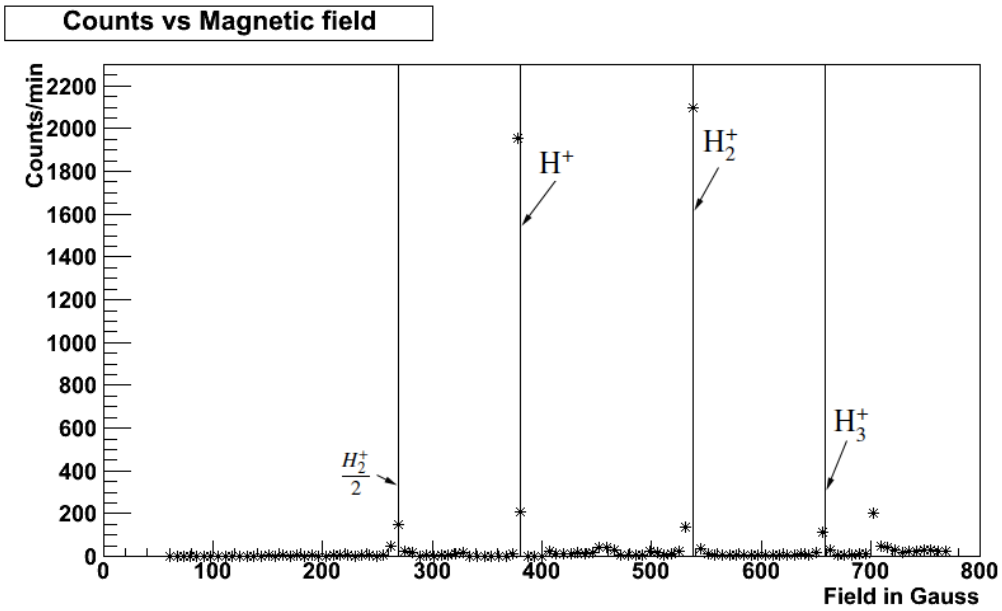

Figure 4.2: MCP rate vs. magnetic field for acceleration voltage 27245 V. The x-axis steps occur in 6.5 Gauss increments. The solid vertical lines are calculated using acceleration voltage using Equation (4.2) in Section 4.4.

the source pressure was 3.2×10^{-5} Torr. The ESA voltages were +550 V and -550 V. The MCP voltage setting was 1800 V, as supplied to the voltage divider box. The discriminator threshold on the MCP signal was set at 0.031 V (reading from the test point on the CAEN fan-in/fan-out module). Data were acquired in 5 μV magnetic field steps, corresponding to steps of 6.5 Gauss, each for 60 s. Individual peaks were not studied in detail during this particular scan. The solid vertical lines in Fig. 4.2 correspond to the calculated peak

locations as summarized in Table 4.1.

A spectrum for an acceleration voltage of 30957 V is shown in Fig. 4.3. In this instance, data are plotted as a function of the Bruker DAC setting ("Bruker units"), and they were acquired in 64-step (DAC setting) intervals (corresponding to about 1 G), each for 20 s. The source arc voltage was 441 V, the source arc current was 4.25 mA, and the source pressure was 6.0×10^{-5} Torr. The ESA voltages were +626 V and -626.5 V. The MCP voltage setting was 1800 V supplied to the voltage divider box; the discriminator threshold was set at 0.031 V (CAEN fan-in/fan-out test point reading).

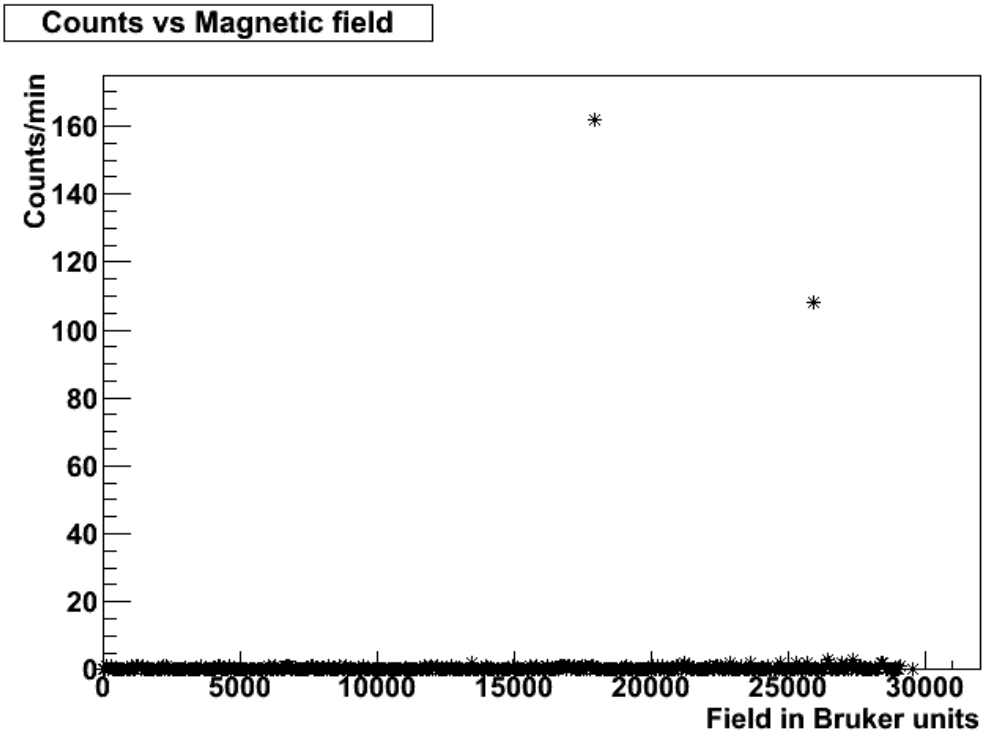

Figure 4.3: Count rate in counts/20s at the MCP detectors vs magnetic field in "Bruker units" with the accelerating voltage set to 30957 V. The leftmost peak corresponds to H^+ and the right peak corresponds to H_2^+

Finer scans at each observable peak in the proton region for various acceleration volt-

ages were performed. Fig. 4.4 shows a more detailed scan of the left-most peak seen at 27245 V in Fig. 4.2, the peak which is due to the dissociation of H_2^+. The full width at half maximum was found to be 8 Gauss. The somewhat broad peak is believed to be due to the more poorly defined kinematics for the dissociation process, though no quantitative estimate of this was attempted. Another source of broadening is dispersion in the range of acceleration potentials available in the ion source, as will be described shortly in relation to the proton peak.

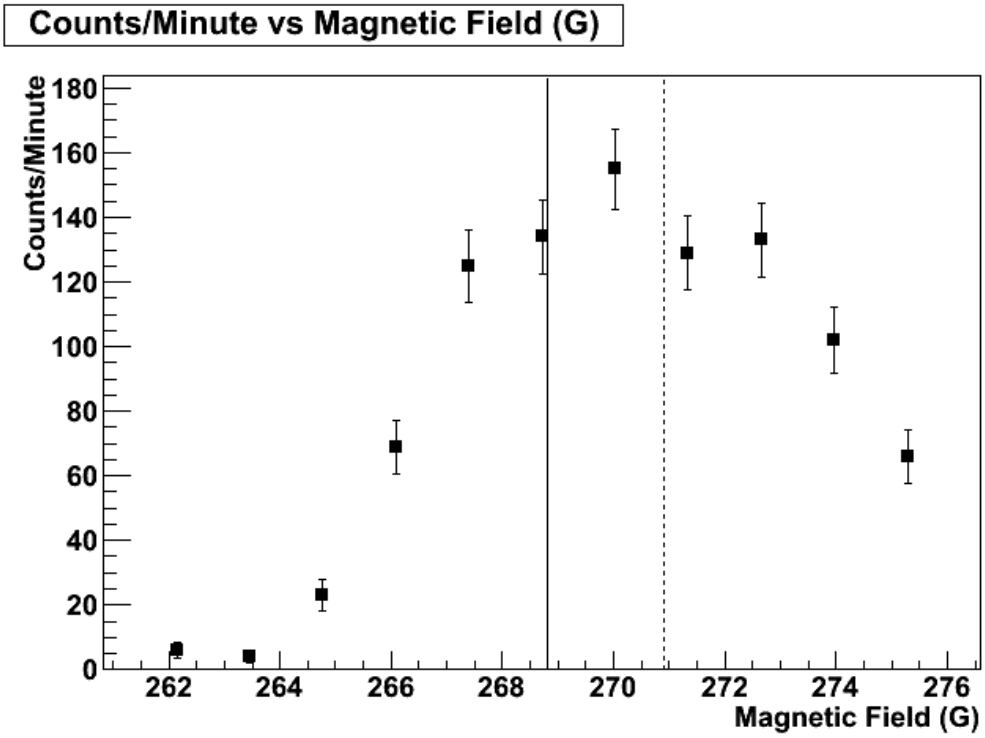

Figure 4.4: Count rate in the mcp detectors in counts/min vs magnetic field for the H_2^+ dissociation peak, for an acceleration voltage of 27245V. The solid line is the calculated peak location using the high voltage setting and the dotted line is the calculated location for the high voltage and the source arc voltage

The peak of most interest for this thesis is of course the proton peak. A finer scan of this shown for 27245 V in Fig. 4.5. The full width at half maximum is of order 1 Gauss,

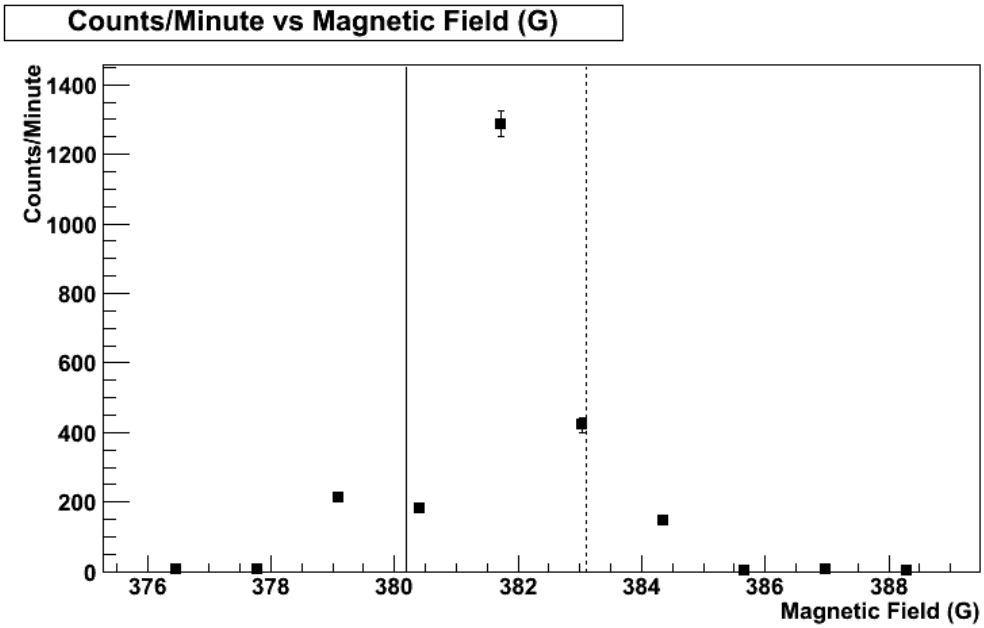

Figure 4.5: Count rate in the MCP detectors in counts/min vs magnetic field for the H^+ peak, acceleration voltage of 27245 V. The solid line is the calculated peak location using the high voltage setting and the dotted line is the calculated location for the high voltage and the source arc voltage.

indicating a resolution of $\sim$ 0.3%. Our ability to probe to better than this was partially limited by the stability of the Hall probe. The maximum number of counts observed on peak in one minute was 1300, while the minimum number of counts was 3 (at the highest field setting shown in the scan). If we take the value 3 as a reasonable estimate of the background counts beneath the proton peak, and the value 1300 as the peak number of counts, then the background beneath the proton peak is no more than 3/1300 or 0.2%.

Our results can be compared to the typical spectrum acquired at (Fig. 4 of Ref. [24]). In the PAFF setup, a distinct double peak is seen, where a subdominant peak at lower energy is experienced due to ions which are emitted with small kinetic energy from their proton source, as opposed to the full arc voltage. In our proton spectrum it is possible that a

similar structure is seen. However, since our arc voltage is more than four times smaller than for PAFF, the difference in peak positions is limited to the 1% level. This is found by comparing two calculated values for the peak location, one including the arc voltage as an additional acceleration, and one not. Both are shown by the solid and dotted vertical lines, respectively, in Fig. 4.5. We therefore believe that the broad tail structure of the peak is in part due to the emission of protons from different parts of the source, and therefore with different acceleration voltages. It is therefore also difficult to discern what portion of the FWHM of the peak is due to spectrometer resolution vs. differing emission energies from the source itself. Unfortunately, slit settings in the spectrometer could not be recorded.

Figs. 4.6 and 4.7 show close-ups of the H_2^+ and H_3^+ peaks, respectively. The H_2^+ peak, in

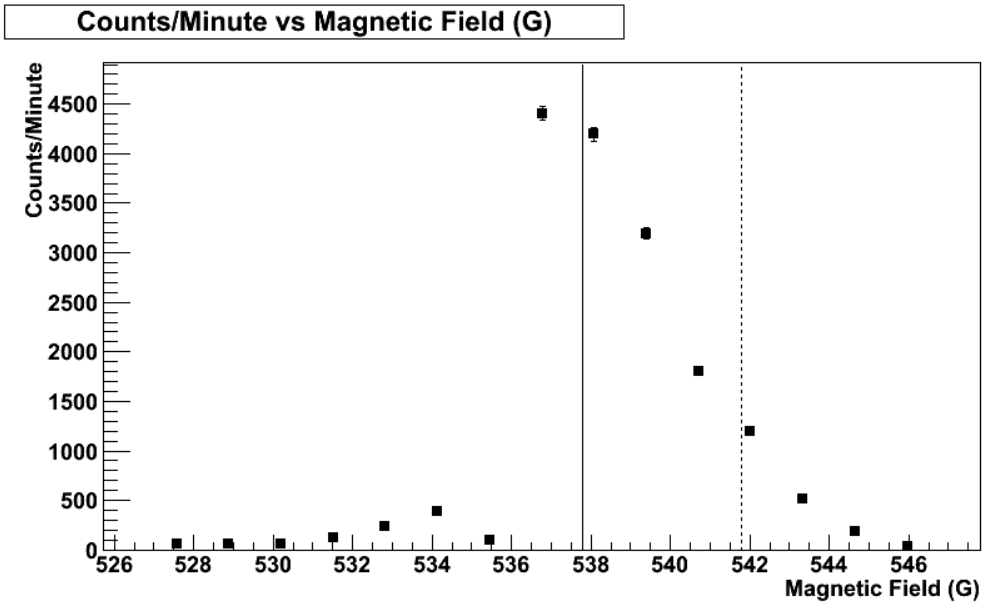

Figure 4.6: Count rate in the MCP detectors in counts/min vs magnetic field for the H_2^+ peak, acceleration voltage of 27245 V. The solid line is the calculated peak location using the high voltage setting and the dotted line is the calculated location for the high voltage and the source arc voltage.

particular, demonstrated an asymmetric shape in these measurements. While the magnitude

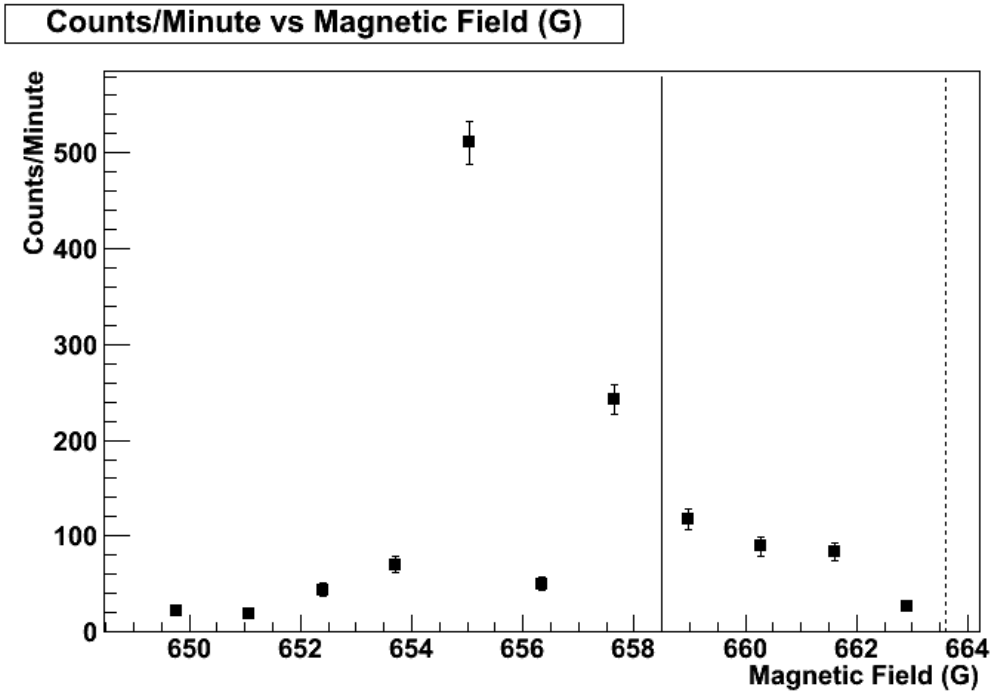

Figure 4.7: Count rate in the mcp detectors in counts/min vs magnetic field for the H_3^+ peak, acceleration voltage of 27245V. The solid line is the calculated peak location using the high voltage setting and the dotted line is the calculated location for the high voltage and the source arc voltage.

of the width is consistent with dispersion ion source emission energies (indicated again by the vertical solid and dashed lines), it is possible that the sharpness of the drop on one side of the peak is due to the presence of apertures. A detailed study of the optics of the spectrometer would have to be carried out to make a more definitive statement. The H_3^+ peak exhibits a similar, but less pronounced, asymmetry, with poorer statistics.

Note on MCP noise and rates of accelerated protons

The MCP detectors were often subject to noise problems throughout the data acquisition period. The result of this is that one should not take the absolute rates as stated in this thesis to be indicative of the true rates of proton emission by the accelerator. Toward the end of the data taking period the MCP noise was observed in more detail leading to a lower discriminator threshold value, which though still not ideal allowed for a higher count rate. Later runs with the adjusted threshold value yielded proton rates of about 200 Hz. Thus we believe the proton rates to be greater than 200 Hz for the spectrometer settings studied.

4.6 Ion Source Results

Tests of ion source performance were performed as a function of various source parameters such as pressure, arc voltage, and arc current.

A schematic graph enabling a description of the operational characteristics of the source, and terminology, is shown in Fig. 4.8. No discharge occurs for small applied voltage and therefore no current flows. As the voltage applied to the source is increased, a stable discharge is eventually generated within the source, where increasing the voltage applied to the source gives rise to a monotonic rise in the discharge current. The transition between the two regions occurs at a voltage that we refer to as the “arc point”. As the voltage is

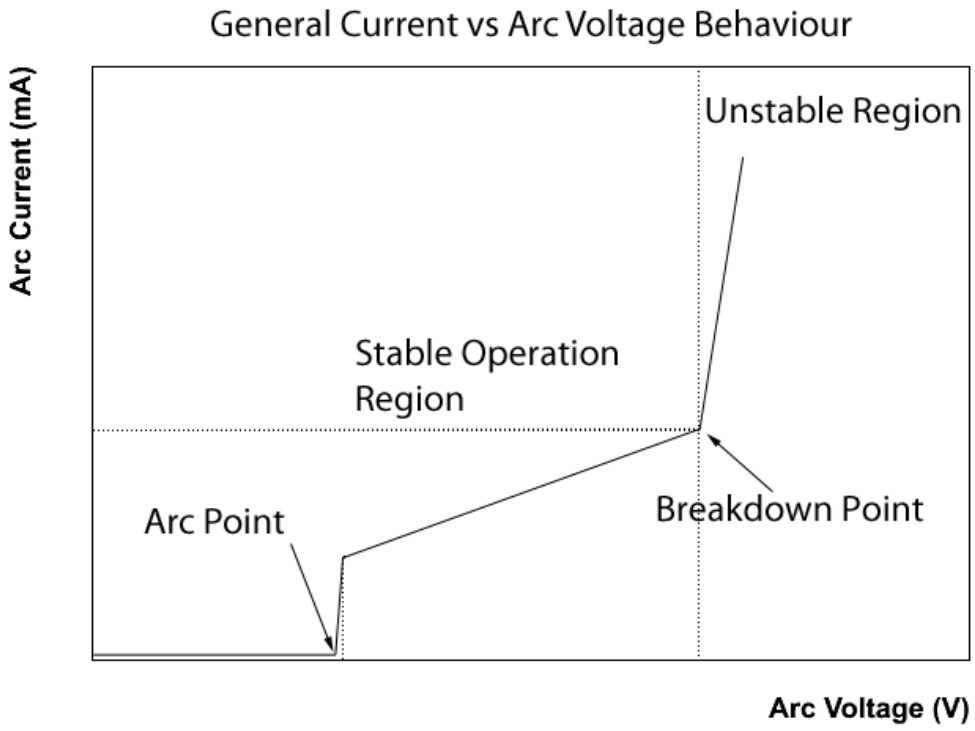

Figure 4.8: A schematic drawing of the general source behaviour in terms of current vs. voltage. The behavior in the various regions of operation is described in the text.

further increased an uncontrolled breakdown occurs and the arc current rises rapidly. The transition to this region is referred to as the "breakdown point".

The locations of the arc point and the breakdown point were characterized as a function of backing line gas pressure by adjusting the needle valve controlling the gas flow into the source. The results are summarized in Table 4.2. A graph of the same data displaying the

Table 4.2: Table of arc and breakdown points for source operation

Backing Pressure (mTorr)	Initial arc point (V)	Breakdown point (V)
55	440	500
60	340	400
70	310	340
80	310	350
90	290	340
100	280	325
150	270	295

trend with pressure is presented in Fig. 4.9.

This early data suffers from two drawbacks. First, only the backing pressure monitored at the exit to the diffusion pumps in the source was monitored. The actual source pressure for these tests varied in the 10^{-6} – 10^{-5} Torr range, as measured at the entrance to one of the diffusion pumps which pumps the source region. A backing pressure of 40 mTorr corresponded to a pressure measured at the entrance to the diffusion pumps of 3×10^{-6} Torr. The other drawback is that insufficient accuracy on the arc current was recorded due to the use of an imprecise current meter. To improve the accuracy of the current measurement in subsequent runs, a 164.5 Ω resistor in series with the source voltage was installed. The voltage drop across the resistor was monitored with a digital voltmeter and allowed for a calculation of the arc current.

The reason for the inclusion of this early data is that it involves the largest range of

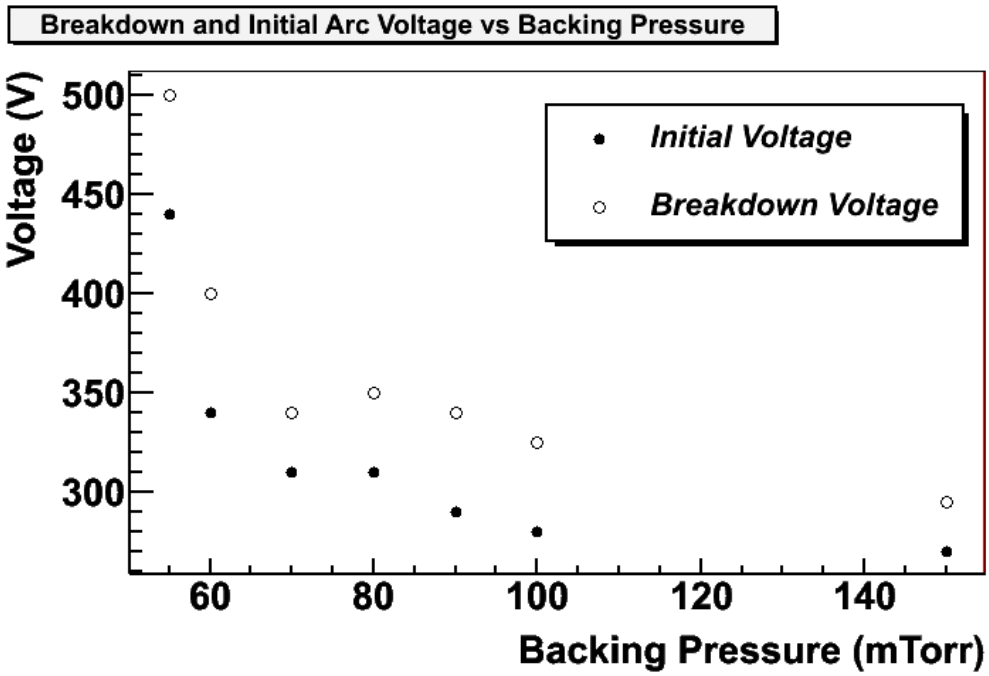

Figure 4.9: Break down voltage (white circles) and initial arc voltage (black circles) as a function of backing pressure measured before the mechanical pump backing the diffusion pumps connected to the source region.

source parameters studied during the data acquisition period. Also, the source performed consistently when this data was taken and provided insight into future source operation.

With the new method of measuring the source current, improved measurements could be made. Fig. 4.10 displays a measurement of the arc current for increasing arc voltage. The arc point is found to be at 560 V and the breakdown point is found at 770 V. The source operating pressure, monitored at the entrance to the diffusion pump using an ion gauge, was 3×10^{-5} Torr. Stable source operating currents of $1 - 2$ mA were observed.

The level of reproducibility of the source operating parameters is apparent from these data: the region of stable operation is considerably higher (in voltage) than for the earlier data. The reason for this is that, in the intervening period, the source region was vented

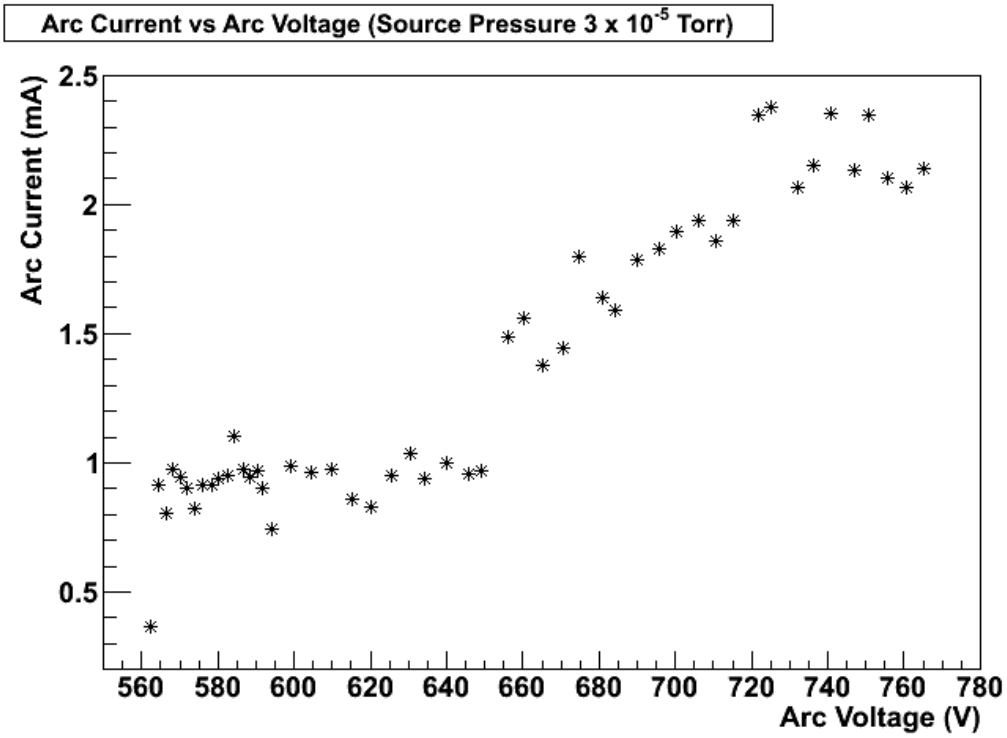

Figure 4.10: Source current vs. applied voltage. The operating parameters are for a source pressure of 3×10^{-5} Torr, an accelerating voltage of 30947 V, ESA settings of ±626 V and a field setting of 321 μV (corresponding to 401 G).

several times, and even had to be cleaned with organic solvents due to a vacuum pump failure. This had an effect on the properties of the surfaces within the source and on the general vacuum quality in the source region. Therefore it is necessary to perform source characterization after venting, repairs to the vacuum system, or cleaning of inner surfaces of the source region.

The source can also be characterized by the current delivered to the experiment, after transport through the entire Manitoba-II mass spectrometer system. This is monitored by the multichannel plate (MCP).

Fig. 4.11 displays a measurement of the MCP rates as a function of arc voltage for data acquired simultaneously with those presented in Fig. 4.10. The ion source parameters are therefore the same as those described in relation to Fig. 4.10. Additionally, since transport through the mass spectrometer system was necessitated, the settings for the accelerator (acceleration potential, ESA, and magnetic field) are reported in the figure caption.

The chief deficiency observed in Fig. 4.11 is that, although the accelerator had been tuned to the proton peak and was operating stably, the signals from the MCP displayed a mere < 40 counts/minute. The reason for this is not poor transport through the machine, but poor efficiency of the MCP at this time. The MCP was suffering from large noise influence due to poor grounding, and therefore the threshold had been raised. Steps were therefore subsequently taken to ensure proper shielding of the MCP signal.

Fig. 4.12 displays a measurement of MCP rate as a function of arc voltage once the noise issue with the MCP had been solved. Once the noise had been reduced, the threshold of the detector could be reduced, and the detected rate increased substantially (to rates in excess of 10 Hz). It is possible that the MCP noise and threshold were still not optimal for these data. Furthermore the MCP rate is related to the true proton rate by an efficiency factor that was not characterized. Nominally this efficiency is given by the detectors open

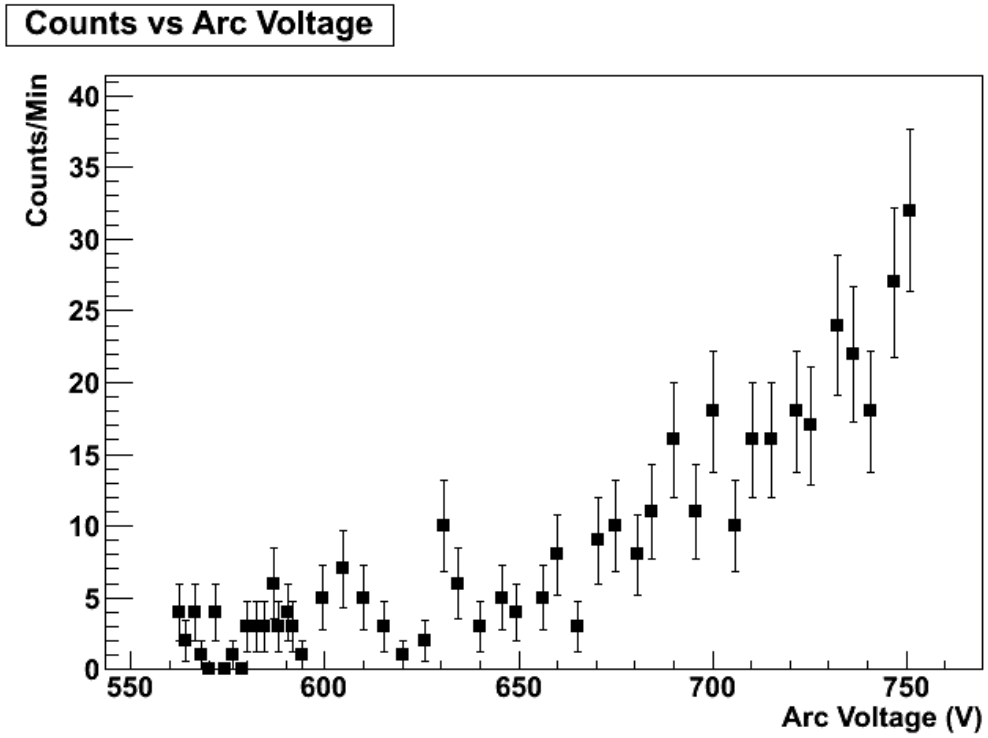

Figure 4.11: MCP rate vs. arc voltage. The operating parameters are for a source pressure of 3×10^{-5} Torr, an accelerating voltage of 30947 V, ESA settings of ±626 V and a field setting of 321 μV (corresponding to 401 G).

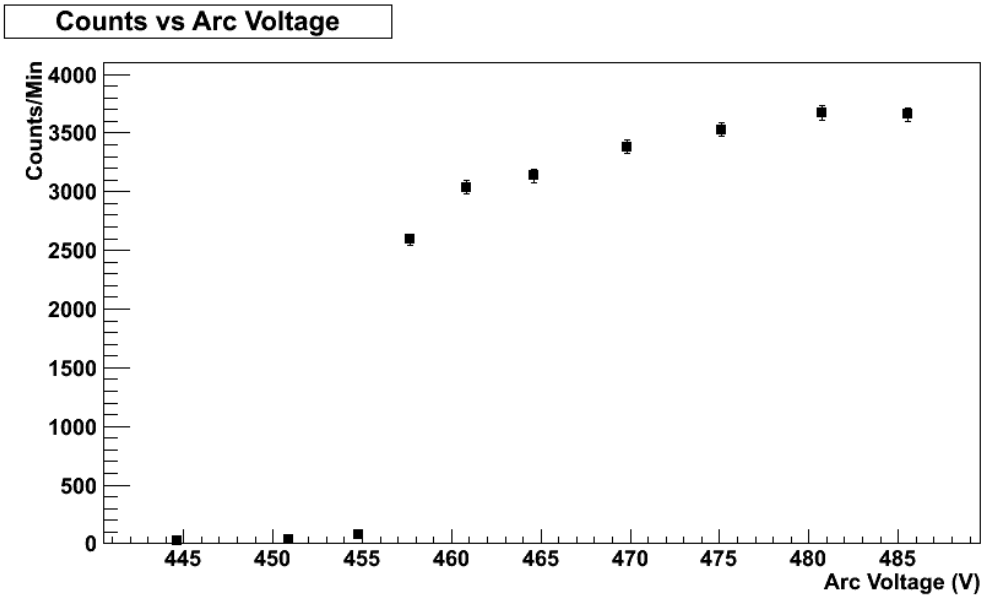

Figure 4.12: Source current vs. arc voltage. The operating parameters are for a source pressure of 6×10^{-5} Torr, an accelerating voltage of 30947 V, ESA settings of ±626 V and a field setting of 321μ V (corresponding to 401 G).

area (open entrance to microchannels) which for our MCPs is 64 %, this is the area of the detector which consists of microchannels. The MCP rate should therefore be taken as a relative measure of the true proton beam current, or a lower bound.

The data in Fig. 4.12 were taken with slightly different machine parameters than those in Fig. 4.11, namely that the source pressure was higher (6×10^{-5} Torr as opposed to 3×10^{-5} Torr). However it is *not* this factor that resulted in the larger MCP rate, it is primarily the improvement of the MCP noise level and the lowering of the discriminator threshold.

For completeness, Fig. 4.13 presents the measurement of the arc current for increasing arc voltage for the source pressure of 6×10^{-5} Torr, acquired simultaneously with the data presented in Fig. 4.11. This indicates that the overall beam current should be a factor of $\sim 2-3$ larger than for the 3×10^{-5} Torr source pressure (comparing with Fig. 4.10). These

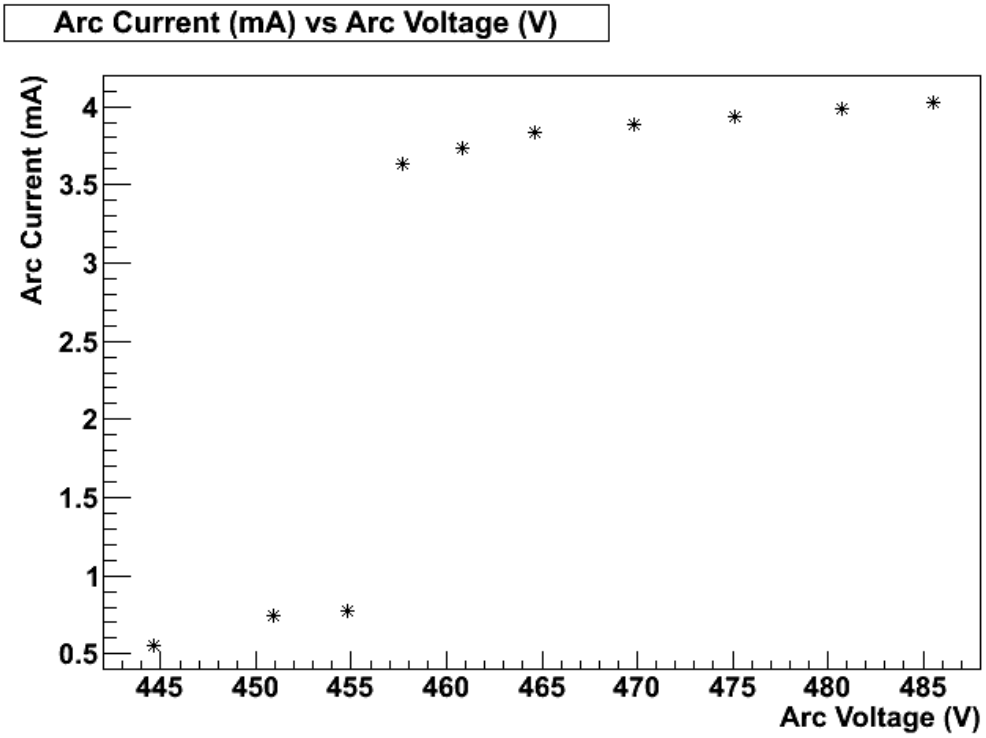

Figure 4.13: Source current vs. applied voltage. The operating parameters are for a source pressure of 6×10^{-5} Torr, an accelerating voltage of 30947 V, ESA settings of ± 626 V and a field setting of 321μ V (401 G).

measurements, for a source pressure of 6×10^{-5} Torr, yielded an arc point of 445 V and a breakdown point of 490 V,

It is interesting to consider the dependence of the MCP count rate with arc current for these data, and this is shown in Fig. 4.14. Stable operating currents in the range 0.5 – 1 mA

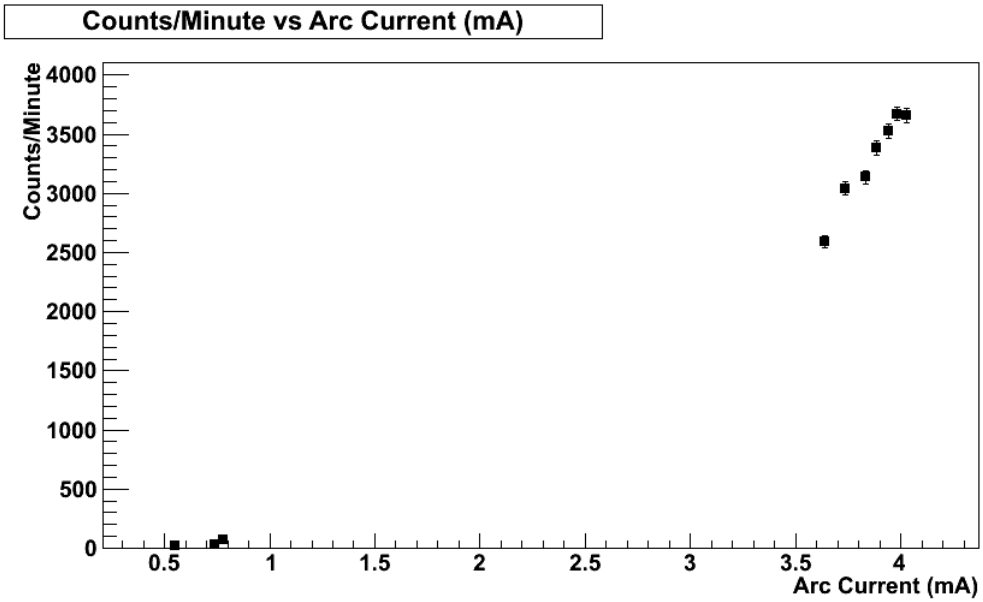

Figure 4.14: MCP rate vs. source arc current, for the same settings as Fig. 4.13.

as well as in the 3.5 – 4 mA range were observed. It is believed that the source is operating stably and producing protons at both current ranges. Presumably the larger current range has occurred when a true arc has been struck within the source. The lower current range must be due to small arcing without full generation of a plasma. Further study would be required to fully diagnose this.

In each current region, the MCP count rate exhibits a linear dependence with arc current. The slope of the dependence in the higher current region is steeper but still linear, also lending credence to its characterization of a plasma from which protons are being more efficiently extracted.

4.7 Silicon tests

Ortec silicon detectors were used in an attempt to identify an incident proton signal. The detector arrangement itself was described in Sections 3.4 and 3.6. We note further that, as a front end and data-acquisition chain, the silicon signal was amplified by an Ortec 109A preamplifier followed by a spectroscopy amplifier. The unipolar output of the spectroscopy amplifier was digitized by a multichannel analyzer. This system was therefore somewhat separate from the MCP acquisition path, for simplicity not employing the MIDAS VME-based acquisition system described in Section 4.3.

Tests of the silicon detectors were performed using an Am-241 source in a dark box in air, which enabled a rough energy calibration of the detector. The source emits two dominant forms of radiation that may be sensed by the silicon detector: a 59.5 keV gamma ray, and 5.5 MeV alpha particle.

In order to select the 60 keV gamma ray, a thin plastic cap was placed over the silicon detector, the cap effectively prevented the alpha particles from ever entering the detector. A spectrum of Am-241 from the dark box with the plastic cap on the silicon detector is presented in Fig. 4.15. The photopeak from the 60 keV gamma ray may be seen. The peak is well-separated from the noise that is seen for lower pulse heights.

Without the plastic cap the alpha particle radiation from the Am 241 deposits its energy in the silicon, this however requires the distance in air between source and detector to be minimal. The results without the plastic cap are presented in Fig. 4.16. The energy loss fluctuations of the alpha particles in air gives rise to the Landau-like spectrum observed by the silicon detector. The relative gain in this case was a factor of ten smaller than the gain for Fig. 4.15, adjusted by a dip switch on the Ortec 109A preamplifier.

The main goal of these tests was to satisfy ourselves that the 60 keV gamma ray from

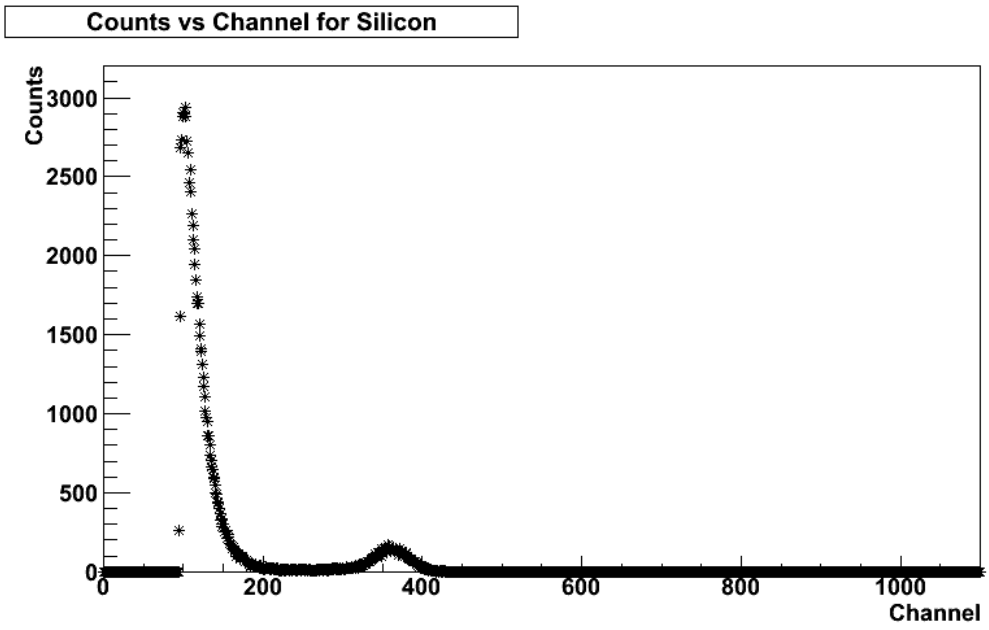

Figure 4.15: Amm-241 spectrum from silicon detector in a dark box, at atmosphere, with a plastic cap on the detector eliminating the alpha radiation. The peak on the right is identified as a 59.5 keV gamma. The peak observed on the left results from noise which is clipped by the digitization threshold of the MCA.

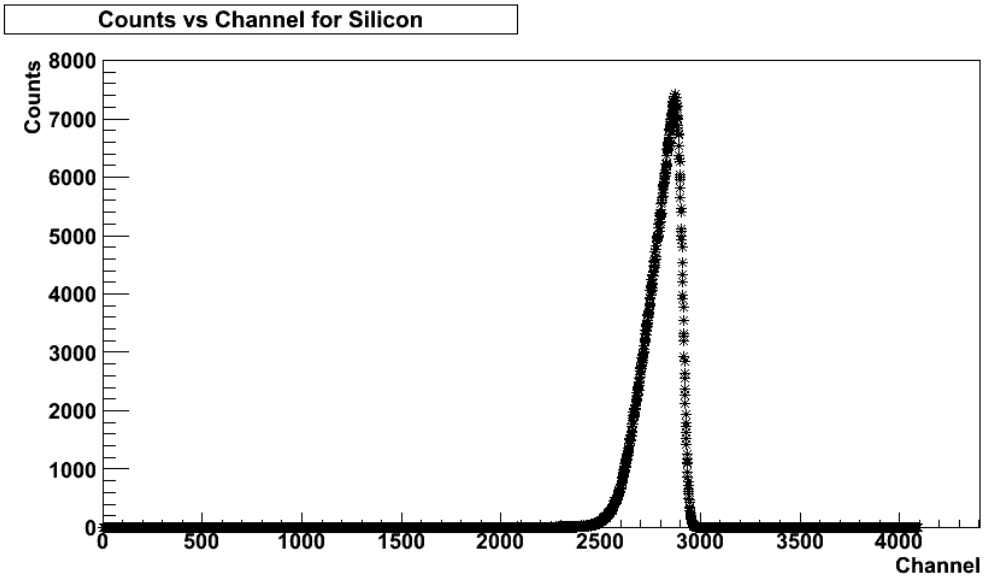

Figure 4.16: Americium 241 spectrum from silicon detector in a dark box, the peak is identified as the 5.5 MeV alpha peak

Am-241 was observable above the noise, and hence that the noise qualities of the system would be sufficient to attempt to expose the detector to 30 keV protons from our accelerator.

4.8 Protons on Silicon

The silicon detector was then mounted on a BNC feedthrough in a location downstream relative to the MCP detector location (described in Sections 3.4 and 3.6). A search for a proton signal on the silicon detectors was then carefully conducted by first obtaining a signal on the MCP detectors then carefully adjusting the field with the MCP removed. An initial signal was observed for an acceleration voltage setting of 30724 V, an arc current of 4 mA, a source arc voltage of 385 V, a source region pressure of 3×10^{-5} Torr and a magnetic field setting of 320.5 μV (400.8 G). This initial proton signal was barely visible above the noise in the silicon detectors, though there was a distinct beam correlated signal.

It was suspected that the beam was missing the silicon detector so beam steering in the form of permanent magnets was used.

Beam steering using permanent magnets was done by placing the magnets next to the beam line before the detector region and adjusting them until a signal was seen on the silicon detectors. Using such steering a strong signal was observed with the settings of: an acceleration voltage of 31054 V, arc current of 4mA, source arc voltage of 450 V, a source region pressure of 5.5×10^{-5} Torr, ESA voltage ± 625 V and a magnet setting 321.7 μ V. Three separate 300 s runs were done: one with a low proton rate obtained by closing the slit after the magnet, one with a higher rate with the after magnet slit removed and a background with gate valves closed. Fig. 4.17 shows the proton spectrum (solid line), higher rate proton spectrum (dotted line) and the background spectrum (finely dotted line) for protons on silicon.

The spectra show that when the proton rate is kept small there is a well defined proton peak located at channel number 79. When the rate was allowed to increase a second broad peak was observed in a region centered around channel number 150, this second peak at about double the channel number of the initial peak is thought to be cases of two protons striking the silicon at the same time. The observation of 31 keV protons on the silicon detectors shows that the proton accelerator achieved its design goals. However better focusing of the beam beyond the magnet will be required for more detailed silicon detector tests.

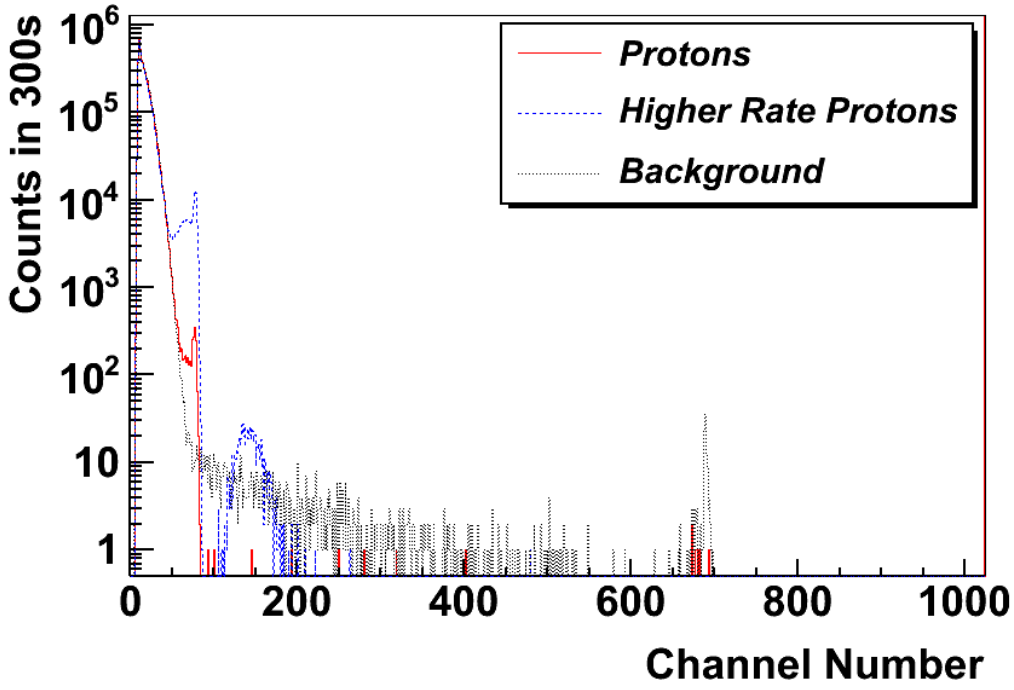

Figure 4.17: The 3 data sets taken were protons, higher rate protons and a background, all three are plotted in this figure and are identified in the legend.

Chapter 5

Conclusion

Future fundamental physics experiments in neutron beta-decay aim to constrain standard model parameters to unprecedented precision. Many of these experiments furthermore aim to constrain parameters that are only accessible with proton detection. Crucial requirements on the efficiency and timing properties of the detector are placed, which depend on the experiment that is being pursued. Often, silicon detectors are selected for the detector solution. These detectors possess a dead layer through which the low energy recoil protons must be accelerated to $\gtrsim$ 30 keV in order to be sensed. A careful characterization of the detector efficiency in light of the dead layer must be conducted in order to ensure highly efficient proton detection.

A 30 keV proton accelerator was designed, created, and commissioned with this goal in mind. Final construction and initial results on the performance of the accelerator are presented in this thesis. The accelerator consists of an ion source, acceleration region, mass spectrometer, and detector region. The main new features are the ion source and detector region; the mass spectrometer is the existing Manitoba II mass spectrometer. The ion source in particular is based on a different technology than typically used in other proton

accelerators, being of the Penning ion generator type, as opposed to the filament type.

Ions produced by the source were analyzed by the mass spectrometer. The chief components of the beam were found to be H^+, H_2^+, H_3^+, and a component arising from dissociation of H_2^+ in flight. All these were expected from previous results from other accelerators constructed elsewhere. Fortunately our excellent mass spectrometer was able easily to distinguish between these species with small contamination. The accelerator produced protons with momentum resolution $\sim$ 1%. The background beneath the proton peak from other sources was limited to $< 0.2\%$ based on counts observed on the sidebands of the peak.

The ion source produced arc currents of order 1-4 mA with a relatively flat behavior over a range of modest arc voltages in the range of 200-800 V. The source operated well with a 1:1 Ar:H (by pressure) mixture, with source pressures in the 10^{-5} Torr range. The source was furthermore found to operate stably over long periods of time. The accelerator achieved proton rates detected by a microchannel plate array in the detector region in excess of 3500 counts/minute. This is sufficient current for the intended use of the accelerator, which is to calibrate large-area silicon detectors of protons resulting from neutron decay in future experiments at the Spallation Neutron Source or elsewhere.

Protons of 31 keV were detected on a silicon detector after beam steering was performed using permanent magnets. This result confirmed that the proton accelerator achieved its design goals and that the protons were detectable by a small silicon detector. It was also observed that beam collimation can have a significant effect on the rate. Crude collimation was achieved by adjusting a slit located after the mass selecting magnet.

In the future, and beyond the scope of this thesis, a variety of tasks will be completed resulting in the use for large-area silicon detector calibration. The accelerator long-term operational stability will be improved. A system to contain large-area silicon detectors and their associated cooled electronics will be developed. A method to focus, collimate,

and divert the proton beam onto different parts the detectors will be developed. A motion mechanism for the detectors is also envisioned so that their surfaces can be scanned through the proton beam maintaining the incident proton angle. A system to test larger proton incident angles is envisioned. Finally, a system to detect secondary electrons emitted from the silicon detector surface is also being considered. This would allow an independent way to calibrate both the efficiency and timing properties of the detector.

Appendix A

Appendix A: Operation

A.1 Operation

A.1.1 Operational overview

Operation of the proton accelerator requires knowing the appropriate startup, source operation, shutdown and basic repair instructions. External to the accelerator a supply of argon and hydrogen gas as well as liquid nitrogen are required, as well a nitrogen gas cylinder may be required to operate the vibration isolation system. The following sections will try to provide a practical and effective overview of the accelerator's use.

A.1.2 Startup

The following startup procedure should be followed when the source region has been vented. If the source region was already at vacuum then the steps for pumping down the source region with the diffusion pump need not be followed.

1. Pressure check: Ensure proper readings for the vacuum: ESA vacuum 1×10^{-6} Torr

or better, Magnet region vacuum 1×10^{-7} Torr or better, 8 in cross region 1×10^{-8} Torr or better and the roughing line vacuum of 0.5×10^{-3} Torr or better.

2. Diffusion pump check: Ensure that the ion gauge for the diffusion pumps when turned on is reading 5×10^{-5} Torr or better, then fill the diffusion pump cold traps with liquid nitrogen. If the source region is not being pumped by the diffusion pumps then follow the instructions in the next sentences. First fill the diffusion pump cold traps with liquid nitrogen. Next ensure the diffusion pump gate valves are closed. Close the backing valve for the diffusion pumps and open the roughing valve to the source to begin roughing out the source chamber. Once the chamber has reached 100×10^{-3} Torr close the roughing valve and then open the diffusion pump backing valve (there should be a brief spike in backing line pressure which will disappear promptly). Then open the diffusion pump gate valve, there should be a spike of the backing pressure to a few hundred mTorr then it should drop back down to about 50 mTorr or better.

3. Gas reservoir check: If there is gas in the reservoir then open the reservoir cylinder and the valve leading to the needle valve. Otherwise close the diffusion pump backing valve, then open the roughing line to the reservoir region this requires the opening of 2 valves. Pump the reservoir until it reaches about 50 mTorr, note that you may have to close the roughing line and reopen the backing valve to the diffusion pumps once the ion gauge pressure rises to above 1×10^{-4} Torr, then when it returns to normal close the backing valve and open the roughing line again. Once the reservoir is roughed then close the roughing line and open the diffusion pump backing valve. Fill the reservoir with gas from the cylinders, start with the argon cylinder and fill the reservoir until about 5 scale markings on the pressure gauge have passed. Then

close the argon valve and fill the reservoir with the same amount of hydrogen, finish by closing the hydrogen valve. This should result in there being a 1-1 hydrogen to argon mixture, based on pressure, available to the needle valve.

4. Generate Plasma: Once there is gas supplied to the needle valve open the needle valve carefully until the ion gauge pressure is seen to increase slightly. Then to create a plasma turn up the arc voltage to about 700 V, once the plasma sparks adjust the voltage and the gas flow until the usual 4 mA arc current is found to be stable.

5. Magnet and ESA: Turn on the ESA power supplies to the desired voltages, switch from standby or input values. Turn on the magnet: Press the green power button on the magnet supply, then press the white button and check that the cooling water is flowing, turn the key from ”local” to ”remote”, start BORIS on the control computer and set the magnetic field as desired. If the magnet stops during operation, hit the red button on the magnet, turn the magnet off, then twist the red button to release it, finally start the magnet again as described above.

6. High Voltage: Once the ESA, magnet and ion source are all operating turn on the accelerating high voltage to the desired value. Flip the main high voltage switch and turn on the high voltage supply, the red light bulb hanging from the cabinet should turn on. Choose set volts by turning the knob then press enter to apply the voltage, then select adjust voltage and you can manually adjust the high voltage via the knob.

7. Maximize beam: Now that everything is on, open the gate valve between the source and the ESA. If things are working then there should be some current being read off of the slits after the ESA. First maximize this value by adjusting the high voltage, the horizontal deflection knob and the vertical deflection knob. Next move the after

magnet slit into the middle location and again adjust the deflection and high voltages to get a maximum, then move the slit back into its open position. Finally open the gate valve to the cross and turn on the desired detector to observe the beam.

A.1.3 Trouble Shooting

There are a large variety of issues that can occur during the operation of the machine. In this section problems and their known best resolution are provided based upon experience.

Vacuum pump problems

There are four main types of pump involved in maintaining a good vacuum: Roughing pumps, Diffusion pumps, Turbomolecular pumps and Ion pumps.

The roughing pumps consist of two types: an oil based pump and an oil free pump. The oil based mechanical pump runs into issues when the oil gets dirty. This can be caused from simple use of the pump or power outage, belt breaking, diffusion pump troubles and more. It is a good practice to check the belt periodically (monthly) to make sure it is not near breaking. The general solution to problems with the roughing pump is to replace the belt if broken and/or to replace the roughing pump oil following the instruction manual for the pump. The dry roughing pumps are more complicated and repair of them in the case of a problem is beyond the scope of this thesis.

The diffusion pumps are fairly resilient pumps which operate in the source region using oil jets to create a vacuum. Problems can occur with the diffusion pumps when there are power outages, as this means that the hot pump's backing vacuum is lost (roughing pump turns off). This can cause overheating of the oil and exposure of hot oil to air causing degradation. The first thing to do if a power outage occurs is check the vacuum. If the

roughing vacuum is reasonable (50 mTorr) then turn the pumps back on by resetting the power (this is done by pressing the red button below where the diffusion pump outlet power switches are located). If the pumps do not work, follow the directions to change the oil in the pumps. Also a wipe down of the cold trap/pump entrance region with Acetone to remove any oil vapor can also help. Usually an oil change and acetone wipe down solves the problem, though it usually takes at least a few days of pumping for the vacuum to be usable without arcing issues.

Problems with the Turbomolecular pumps are beyond this section, careful operation of these pumps is essential.

The ion pumps outgas considerably when initially turned on. It may be necessary to restart them multiple times in order for them to stay running. A solution to this problem is to replace the plates in which the ions are implanted. Information on how to do this should be found elsewhere.

Bibliography

[1] H. Abele, "The neutron. Its properties and basic interactions," Prog. Part. Nucl. Phys. **60**, 1 (2008).

[2] J. S. Nico and W. M. Snow, "Experiments in Fundamental Neutron Physics," Ann. Rev. Nucl. Part. Sci. **55**, 27 (2005).

[3] J.-M. Yang, M. S. Turner, G. Steigman, D. Schramm, and K. A. Olive, "Primordial Nucleosynthesis: A Critical Comparison of Theory and Observation," Astrophys. J. **281**, 493 (1984).

[4] E. G. Adelberger, S. M. Austin, J. N. Bahcall, A. B. Balantekin, G. Bogaert, L. S. Brown, L. Buchmann, F. E. Cecil, A. E. Champagne, L. de Braeckeleer, et al., "Solar fusion cross sections," Rev. Mod. Phys. **70**, 1265 (1998).

[5] G. J. Mathews, T. Kajino, and T. Shima, "Big bang nucleosynthesis with a new neutron lifetime," Phys. Rev. D **71**, 021302 (2005).

[6] I. Towner and J. Hardy, "The evaluation of V_{ud} and its impact on the unitarity of the Cabibbo-Kobayashi-Maskawa quark-mixing matrix," Rept. Prog. Phys. **73**, 046301 (2010).

[7] J. Beringer, J. F. Arguin, R. M. Barnett, K. Copic, O. Dahl, D. E. Groom, C. J. Lin, J. Lys, H. Murayama, C. G. Wohl, et al. (Particle Data Group), "Review of particle physics," Phys. Rev. D **86**, 010001 (2012).

[8] M. J. Ramsey-Musolf, "Nuclear β decay, atomic parity violation, and new physics," Phys. Rev. D **62**, 056009 (2000).

[9] A. Kurylov and M. J. Ramsey-Musolf, "Charged current universality in the minimal supersymmetric standard model," Phys. Rev. Lett. **88**, 071804 (2002).

[10] S. Profumo, M. J. Ramsey-Musolf, and S. Tulin, "Supersymmetric contributions to weak decay correlation coefficients," Phys. Rev. D **75**, 075017 (2007).

[11] J. D. Jackson, S. B. Treiman, and H. W. Wyld, "Possible tests of time reversal invariance in beta decay," Phys. Rev. **106**, 517 (1957).

[12] W. Wilburn et al., "Measurement of neutron decay parameters – The abBA experiment," J. Res. Natl. Inst. Stand. Technol. **110**, 389 (2005).

[13] R. Maisonobe et al. (The aSPECT Collaboration), in *"Neutron β-decay study with the spectrometer aSPECT", presented at the "Cargèse Interational School on QED & Quantum Vacuum, Low Energy Frontier"* (Cargèse, Corsica, France, April 16-27, 2012).

[14] B. Märkisch, H. Abele, D. Dubbers, F. Friedl, A. Kaplan, H. Mest, M. Schumann, T. Soldner, and D. Wilkin, "The new neutron decay spectrometer Perkeo III," Nucl. Instrum. Meth. A **611**, 216 (2009).

[15] S. Sjue et al. (The UCNB Collaboration), in *"The UCNB experiment: progress toward the measurement of electron-proton coincidences from the beta decay of polarized,*

ultracold neutrons", presented at the "APS April Meeting 2013" (Denver, Colorado, USA, April 13-16, 2013).

[16] T. E. Chupp, R. L. Cooper, K. P. Coulter, S. J. Freedman, B. K. Fujikawa, A. García, G. L. Jones, H. P. Mumm, J. S. Nico, A. K. Thompson, et al., "Search for a *t*-odd, *p*-even triple correlation in neutron decay," Phys. Rev. C **86**, 035505 (2012).

[17] D. Dubbers, H. Abele, S. Baeßler, B. Märkisch, M. Schumann, T. Soldner, and O. Zimmer, "A clean, bright, and versatile source of neutron decay products," Nucl. Instrum. Meth. A **596**, 238 (2008).

[18] F. E. Wietfeldt, B. M. Fisher, C. Trull, G. L. Jones, B. Collet, L. Goldin, B. G. Yerozolimsky, R. Wilson, S. Balashov, Y. Mostovoy, et al., "A method for an improved measurement of the electronantineutrino correlation in free neutron beta decay," Nucl. Instrum. Meth. A **545**, 181 (2005).

[19] S. Materne, R. Picker, I. Altarev, H. Angerer, B. Franke, E. Gutsmiedl, F. Hartmann, A. Mller, S. Paul, and R. Stoepler, "Penelope – on the way towards a new neutron lifetime experiment with magnetic storage of ultra-cold neutrons and proton extraction," Nucl. Instrum. Meth. A **611**, 176 (2009).

[20] J. S. Nico, M. S. Dewey, D. M. Gilliam, F. E. Wietfeldt, X. Fei, W. M. Snow, G. L. Greene, J. Pauwels, R. Eykens, A. Lamberty, et al., "Measurement of the neutron lifetime by counting trapped protons in a cold neutron beam," Phys. Rev. C **71**, 055502 (2005).

[21] D. Pocanic et al. (Nab Collaboration), "Nab: Measurement Principles, Apparatus and Uncertainties," Nucl. Instrum. Meth. A **611**, 211 (2009).

[22] "Proposal for an Experiment at the Spallation Neutron Source, Precise Measurement of the Neutron Beta Decay Parameters *a* and *b*, The Nab Experiment", J. D. Bowman and D. Pocanic spokespersons (2007), URL http://nab.phys.virginia.edu/nab_proposal.pdf.

[23] S. Baessler et al. (Nab collaboration), "Neutron Beta Decay Studies with Nab," (2012), arXiv:1209.4663.

[24] A. Müller, F. Hartmann, S. Paul, G. Petzoldt, R. Picker, M. Simson, H.-F. Wirth, O. Zimmer, and W. Carli, "PAFF, a low-energy, low-flux proton accelerator for detector tests," Nucl. Instrum. Meth. A **582**, 395 (2007).

[25] S. A. Hoedl, "Novel Proton Detectors, Ultra-Cold Neutron Decay and Electron Backscattering", Ph.D. thesis, Princeton University (2003).

[26] J. L. Rovey, B. P. Ruzic, and T. J. Houlahan, "Simple Penning ion source for laboratory research and development applications," Rev. Sci. Instrum. **78**, 106101 (2007).

[27] R. Herzog, "Ionen- und elektronenoptische Zylinderlinsen und Prismen. I," Z. Phys. **89** (1934).

[28] H. E. Duckworth, R. C. Barber, and V. S. Venkatasubramanian, *Mass Spectroscopy* (Cambridge University Press, Cambridge, United Kingdom, 1990).

[29] R. Barber, R. Bishop, H. Duckworth, J. Meredith, F. Southon, P. van Rookhuyzen, and P. Williams, "A high resolution mass spectrometer for atomic mass determinations," Rev. Sci. Instrum. **42**, 1 (1971).

[30] W. R. Leo, *Techniques for Nuclear and Particle Physics Experiments: A How-To Approach* (Springer-Verlag GmbH, 1994).

[31] G. F. Knoll, *Radiation detection and measurement* (Wiley, 2000).

[32] The abBA design was fabricated by Micron Semiconductor Ltd., 1 Royal Buildings, Marlborough Road, Lancing Business Park, Lancing, Sussex, BN15 8SJ, England, URL http://www.micronsemiconductor.co.uk.

[33] The nickel-coated neodymium circular magnets used were 1/2" ϕ and 1/8" thick, of nine pound magnetic strength, and were purchased from Lee Valley, 1395 Ellice Avenue, Winnipeg, MB, R3G 0G3, URL http://leevalley.com.

[34] Part number MCP 24/12/10/12 D 40:1 available from Photonis USA, Inc., P.O. Box 1159, Sturbridge, MA 01518, USA, URL http://www.photonis.com.

[35] M. Berger, J. Coursey, M. Zucker, and J. Chang, "ESTAR, PSTAR, and ASTAR: Computer Programs for Calculating Stopping-Power and Range Tables for Electrons, Protons, and Helium Ions (version 1.2.3)," (2005), URL http://physics.nist.gov/Star.

[36] The MIDAS data-acquisition software has been jointly developed by TRIUMF, Canada's National Laboratory for Particle and Nuclear Physics, in Vancouver, Canada, and the Paul-Scherrer Institut, in Villigen, Switzerland., URL http://midas.triumf.ca.

[37] CAEN Technologies, Inc., 1140 Bay Street, Suite 2C, Staten Island, NY 10305, USA, URL http://www.caen.it.

[38] ROOT, An Object-Oriented Data Analysis Framework, URL http://root.cern.ch.

[39] Eds. P.J. Linstrom and W.G. Mallard, *NIST Chemistry WebBook, NIST Standard Reference Database Number 69* (National Institute of Standards and Technology, Gaithersburg MD, retrieved March 19, 2013), URL `http://webbook.nist.gov`.